Central and Eastern U.S. Surface Pressure Variations Derived from the USArray Network

ALEXANDER A. JACQUES, JOHN D. HOREL, AND ERIK T. CROSMAN

Department of Atmospheric Sciences, University of Utah, Salt Lake City, Utah

FRANK L. VERNON

Scripps Institution of Oceanography, University of California, San Diego, La Jolla, California

(Manuscript received 26 August 2014, in final form 8 December 2014)

ABSTRACT

Large-magnitude pressure signatures associated with a wide range of atmospheric phenomena (e.g., mesoscale gravity waves, convective complexes, tropical disturbances, and synoptic storm systems) are examined using a unique set of surface pressure sensors deployed as part of the National Science Foundation EarthScope USArray Transportable Array. As part of the USArray project, approximately 400 seismic stations were deployed in a pseudogrid fashion across a portion of the United States for 1–2 yr, then retrieved and redeployed farther east. Surface pressure observations at a sampling frequency of 1 Hz were examined during the period 1 January 2010–28 February 2014 when the seismic array was transitioning from the central to eastern continental United States. Surface pressure time series at over 900 locations were bandpass filtered to examine pressure perturbations on three temporal scales: meso- (10 min–4 h), subsynoptic (4–30 h), and synoptic (30 h–5 days) scales.

Case studies of strong pressure perturbations are analyzed using web tools developed to visualize and track tens of thousands of such events with respect to archived radar imagery and surface wind observations. Seasonal assessments of the bandpass-filtered variance and frequency of large-magnitude events are conducted to identify prominent areas of activity. Large-magnitude mesoscale pressure perturbations occurred most frequently during spring in the southern Great Plains and shifted northward during summer. Synoptic-scale pressure perturbations are strongest during winter in the northern states with maxima located near the East Coast associated with frequent synoptic development along the coastal storm track.

1. Introduction

Large-amplitude surface pressure perturbations are produced by a wide variety of high-impact atmospheric phenomena (Koppel et al. 2000; Nappo 2002; Sutherland 2010). Measurements of surface barometric pressure have been used to identify and follow propagating atmospheric systems on spatial and temporal scales ranging from turbulence (e.g., Viana et al. 2010) to multiyear oscillations (e.g., Jones et al. 2003). As summarized by Mass and Madaus (2014), surface pressure observations have fewer siting and measurement issues than observations of temperature or wind. Surface pressure is also more readily assimilated into research and operational models (Whitaker et al. 2004; Dirren et al. 2007; Wheatley and Stensrud 2010). As discussed by Madaus et al. (2014), assimilating densely spaced surface pressure observations shows promise for improving future mesoscale analyses and forecasts.

Numerous studies have relied on pressure observations to catalogue and examine meteorological events. Sea level pressure analyses derived from surface pressure observations have often been used to produce climatologies of synoptic storm tracks (Reitan 1974; Zishka and Smith 1980). More recent climatologies of synoptic storm tracks rely on pressure data derived from numerical model reanalyses (Thomas and Martin 2007; Nieto Ferreira et al. 2013). Pressure tendency (i.e., the change in pressure over a specified duration) has been used frequently to identify preferred geographical locations for cyclogenesis and anticyclogenesis (Sanders and Gyakum 1980; Krueger and von Storch 2012).

While the pressure perturbations associated with internal waves are often viewed as noise for large-scale

Corresponding author address: Alexander A. Jacques, Department of Atmospheric Sciences, University of Utah, 135 South 1460 East, Rm. 819, Salt Lake City, UT 84112.
E-mail: alexander.jacques@utah.edu

DOI: 10.1175/MWR-D-14-00274.1

weather systems (Sutherland 2010), an extensive literature base exists on the theoretical, observational, and modeling of pressure perturbations resulting from a wide array of physical processes. The highest impact pressure perturbations occurring over space and time scales less than those of large weather disturbances are usually gravity waves associated with intense convection, and many analyses of the spatiotemporal evolution of these waves have occurred in the last several decades following T. Fujita's mesoanalyses of barograph traces using time-to-space data reduction techniques (Fujita and Brown 1958; Koch and Saleeby 2001; Johnson 2001). However, as reviewed by Wei and Zhang (2014), gravity waves and their associated pressure perturbations can also result from topographic effects, density gradients, shear instabilities, and geostrophic adjustments. In addition to gravity waves, localized or regional pressure gradients are also generated by mesoscale high and low pressure disturbances, differential heating of land surfaces, diurnal tides, and persistent flow over terrain.

The overlapping temporal scales within which these pressure perturbations and associated phenomena occur include the following:

- Less than 20 min: high-frequency internal gravity waves resulting from shear layers, horizontal convective rolls, katabatic flows, and other boundary layer phenomena (Tian et al. 2004; Adams-Selin and Johnson 2010; Viana et al. 2010);
- 5 min–4 h: propagating gravity waves associated with individual convective storms and associated cold pools, mesohighs and wake lows, bow echoes, derechos, and other mesoscale disturbances (Crook 1988; Engerer et al. 2008; Metz and Bosart 2010);
- 2–12 h: differential heating of land and water surfaces (Novak and Colle 2006), elevated terrain (Geerts et al. 2008), long-lived mesoscale gravity waves and inertia–gravity waves, cold fronts, or drylines associated with large synoptic disturbances (Jewett et al. 2003; Bosart et al. 1998), or prolonged flow over a topographic barrier (Gaberšek and Durran 2006); and
- 12–24 h: diurnal and semidiurnal migrating thermal tides due to diurnal heating (Dai and Wang 1999; Li and Smith 2010).

While many of the phenomena mentioned above tend to occur largely unnoticed, large-amplitude gravity waves, wake lows, and other mesoscale convective systems (MCSs) leading to severe weather have received much attention during recent decades (Ramamurthy et al. 1993; Coleman and Knupp 2009; Coleman and Knupp 2010; Adams-Selin and Johnson 2013). A mix of microbarograph traces and pressure observations at hourly or longer intervals have been the most common tools available to study such events (Bosart et al. 1998).

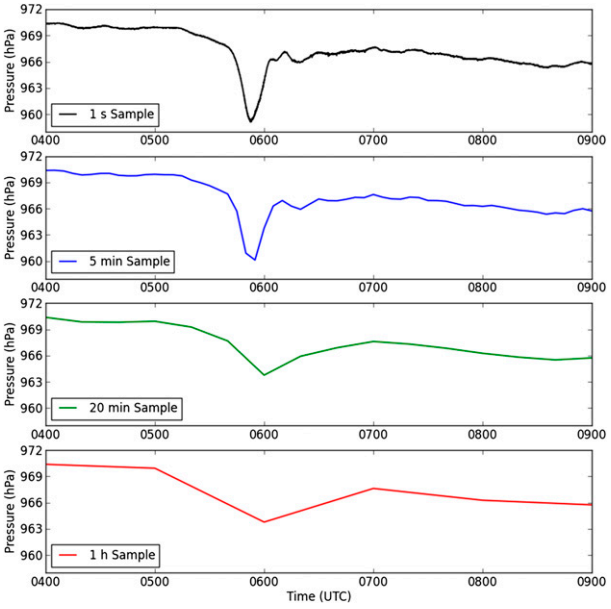

FIG. 1. Pressure sampled at 1 Hz (black), 5 min (blue), 20 min (green), and hourly (red) from USArray station J41A (Loganville, WI) during 0400–0900 UTC 11 Apr 2013.

While extensive research has been conducted regarding the dynamics and evolution of specific high-impact, long-lived mesoscale gravity wave events, relatively few studies have looked at the occurrence of pressure perturbations over broader spatial and temporal scales. Koppel et al. (2000) conducted a 25-yr climatology of large pressure perturbations over the conterminous United States, but were limited by 1-h sampling intervals, which likely underestimated the frequency of occurrence of these features. Figure 1 illustrates the importance of sampling pressure perturbations at high frequency for a large-amplitude gravity wave event on 17 April 2013 for which sampling at 20-min or 1-h intervals fails to capture the primary wave signature.

Various signal processing techniques have been relied upon to isolate discrete or recurring pressure perturbations. Harmonic analysis has been utilized to determine the magnitude and phase of the diurnal, semidiurnal, and terdiurnal cycles (Mass et al. 1991; Ray and Poulose 2005; Li and Smith 2010). Bandpass-filtering techniques were utilized by Koch and O'Handley (1997) as well as Koch and Saleeby (2001) to isolate pressure perturbations coincident with mesoscale gravity waves using pressure observations at 5-min intervals, which as shown in Fig. 1, provide a reasonable reconstruction of gravity waves in pressure time series. Wavelet analysis techniques to extract discrete events in time and space are

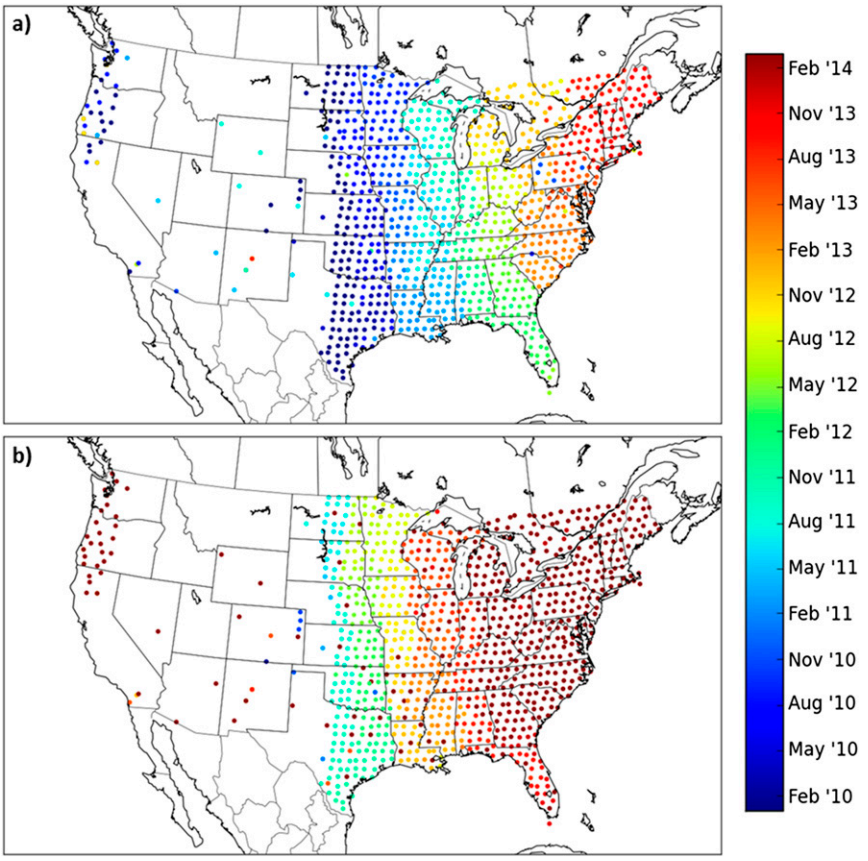

FIG. 2. USArray seismic station locations from 1 Jan 2010 to 28 Feb 2014. Marker colors denote the (a) first and (b) last date of pressure observations.

common as well (Grivet-Talocia and Einaudi 1998; Grivet-Talocia et al. 1999). However, wavelet techniques rely on specifying the expected pressure fluctuation pattern to cast as the mother wavelet, which is difficult to define generally (Torrence and Compo 1998).

This research takes advantage of the deployment beginning in 2010 of pressure sensors on the National Science Foundation sponsored EarthScope USArray Transportable Array (TA; Tytell et al. 2011; Vernon et al. 2011; Vernon et al. 2012). Very high temporal resolution (1 Hz) surface pressure data for roughly 2-yr periods are available at stations separated by ~70 km in the central and eastern portions of the United States and southern Canada. An extensive set of web tools have been developed to interactively examine these data (see http://meso1.chpc.utah.edu/usarray/).

The objective of this study is to analyze the frequency and amplitude of pressure perturbations as a function of location and season at each TA observing site. Bandpass filters applied to the pressure data allow large-amplitude mesoscale, subsynoptic, and synoptic pressure signatures to be examined. Case studies of high-impact events demonstrate the capabilities of the TA 1-Hz pressure surface pressure network to capture the relevant spatiotemporal evolution of these events.

2. Data and methods

a. USArray TA surface pressure observations

The USArray TA in situ network was developed as part of an EarthScope project to study seismic activity across the continental United States (Yang and Ritzwoller 2008; Pavlis et al. 2012). The project began in 2004 with stations placed across the western United States using a pseudogrid concept, with average spacing of about 70 km between locations. Stations report for a period of 1–2 yr, then are retrieved and redeployed as new stations east of the existing grid. This method of station deployment and retrieval produces a temporal ''rolling appearance'' of the array over several years. While only seismic sensors were installed as the array progressed from the Pacific coastline across the west, atmospheric pressure sensors were added to stations that were redeployed over the central United States beginning in 2010 (Fig. 2). As described by de Groot-Hedlin et al. (2014), stations were initially

TABLE 1. Observation and quality control statistics for USArray 1-Hz pressure observations from 1 Jan 2010 to 28 Feb 2014.

Metric	Value
Individual stations	997
Total 1-Hz observations collected	48 358 325 315
Total 1-Hz observations retained post-QC	47 200 863 231
Total 1-Hz observations retained post-QC percentage	97.61%
Median station active period	615.5 days
Median percentage of expected observations	99.84%
Median percentage of observations retained post-QC	99.79%

equipped with less expensive MicroElectro-Mechanical (MEMS) pressure sensors (0.015-hPa resolution, 1.5-hPa accuracy, 1.0 hPa yr^{-1} stability). Additional Setra-278 barometric pressure sensors (0.01-hPa resolution, 0.5–1.0-hPa accuracy, 0.1 hPa yr^{-1} stability) were installed from late 2010 into 2011. Both sensors were enclosed within the main vault of the station that was placed slightly underground for seismometer housing, with tubing extending from the sensors to the surface to allow for adequate sampling of the atmospheric pressure. Readings from the MEMS pressure sensors were initially fetched until the Setra-278 units were installed, with Setra-278 observations taking priority over the MEMS once they were active due to their better accuracy, resolution, and long-term stability.

The combination of high-resolution and fast response time allows the pressure measurements to be collected at high sampling rates (including 1 and 40 Hz) for seismic applications. Real-time communications allow the observations to be received by the Scripps Institution of Oceanography Array Network Facility (ANF) and then transmitted to the Incorporated Institutions of Seismology (IRIS) with minimal latency. Through the IRIS web service products, 1-Hz pressure observations from 1 January 2010 to the present have been retrieved for all USArray stations.

Figure 2 depicts the first and last date within the 1 January 2010–28 February 2014 window during which pressure observations were available for this study at the over 900 unique station locations. In general, stations across the central United States were active during 2010–11, the upper Midwest and Southeast from late 2011 to early 2013, and farther east toward New England and southern Canada during 2013–14. Since 1 March 2012, the 1-Hz data have been processed into 5-min averages, made available publicly with minimal latency via MesoWest (Horel et al. 2002), and transmitted via the NOAA Meteorological Automated Data Ingest System (MADIS) to National Weather Service (NWS) field offices and the National Centers for Environmental Prediction (NCEP) for nowcasting and operational numerical weather prediction.

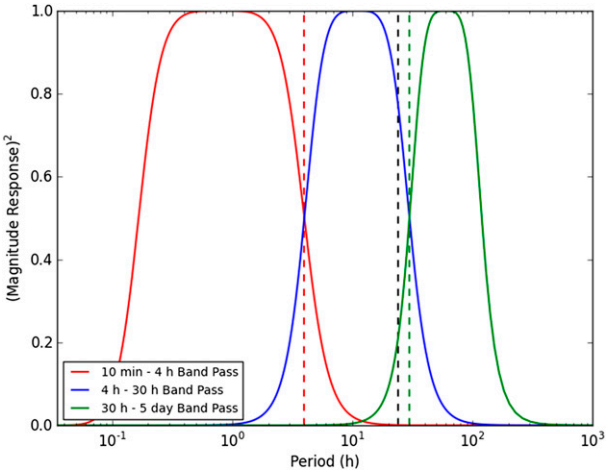

FIG. 3. Period (h) vs squared magnitude response for the meso- (red), subsynoptic- (blue), and synoptic-scale (green) bandpass filters applied to the pressure observations. Vertical lines denote 4-h (red dashed), 24-h (black dashed), and 30-h (green dashed) periods.

b. *Quality control*

Several steps were employed to flag the small amount of erroneous 1-Hz pressure data and to avoid introducing spurious signals resulting from filtering across

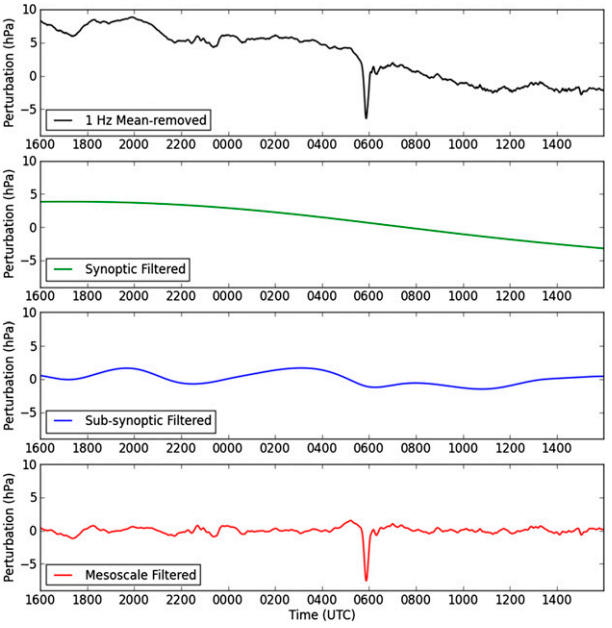

FIG. 4. 1-Hz pressure data (black) and synoptic- (green), subsynoptic- (blue), and mesoscale (red) filtered pressure data for USArray station J41A (Loganville, WI) during 1600 UTC 10 Apr–1600 UTC 11 Apr 2013. The mean derived from the entire station time series was subtracted from the 1-Hz data.

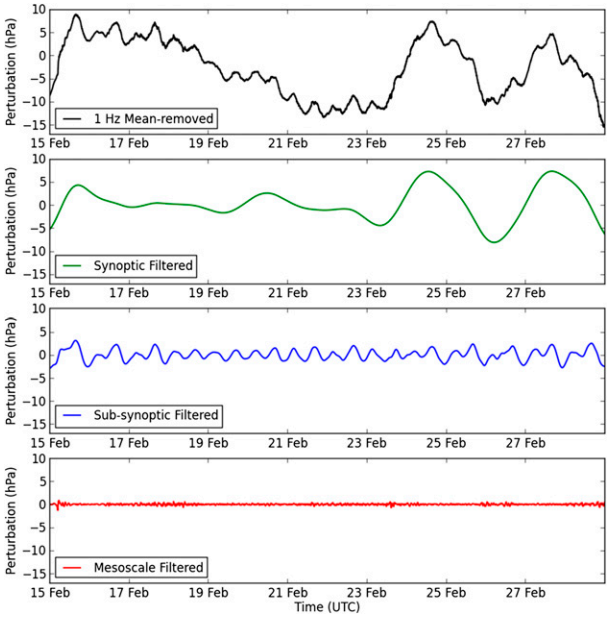

FIG. 5. As in Fig. 4, but for USArray station O35Z (Hargill, TX) from 0000 UTC 15 Feb to 0000 UTC 1 Mar 2010.

data gaps. First, periods of missing data exceeding 5 min were identified and no interpolation was performed to fill in those missing periods. Second, large pressure signals not plausible for atmospheric phenomena of interest in this study were identified. For example, short-duration power outages, pressure sensor "warm up" signatures, and external siting factors occasionally produced large discontinuous changes. Pressure changes exceeding $2\,\mathrm{hPa\,s^{-1}}$ were immediately flagged as suspect, while rates exceeding $2\,\mathrm{hPa\,min^{-1}}$ required further subjective examination on a case-by-case basis. Although pressure change rates exceeding these thresholds could occur as a result of extreme local weather events (e.g., tornadoes or dust devils), sampling such events would be extremely rare, given the large horizontal spacing of the sensor array. Third, bulk statistics (range, variance, etc.) for each station time series over seasonal and annual periods were examined for both pressure and derived altimeter setting using available elevation metadata. Seasons were defined as December–January–February (DJF), March–April–May (MAM), June–July–August (JJA), and September–October–November (SON) periods. These statistics helped to identify stations with problems ranging from improper installation, sensor programming (voltage multiplier or offset issues), or metadata inaccuracies. Finally, subjective quality control was required for some blatantly spurious pressure signals that were not flagged by the objective procedures.

Table 1 provides summary statistics for the total number of 1-Hz observations collected and quality

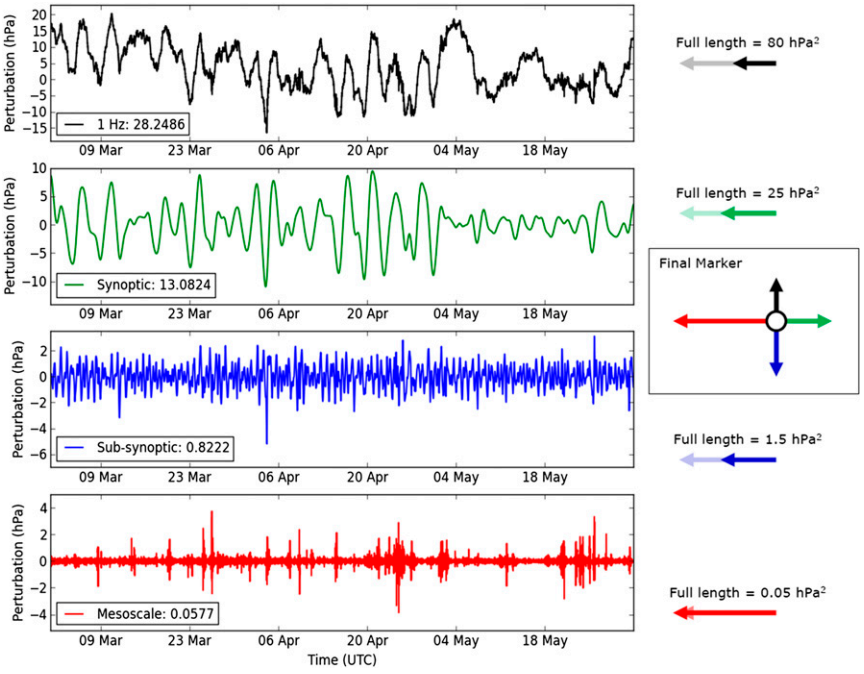

FIG. 6. Time series as in Fig. 4 for USArray station T37A (Cheneyville 1850, KS) for the entire 2011 spring season (MAM). The variance ($\mathrm{hPa^2}$) is provided in the legend for each time series. Vectors corresponding to the variance magnitudes are shown on the right (solid vectors) along with the corresponding "unit length" variance values (translucent vectors). The four vectors are then combined in a compass format for the final marker shown to the middle right.

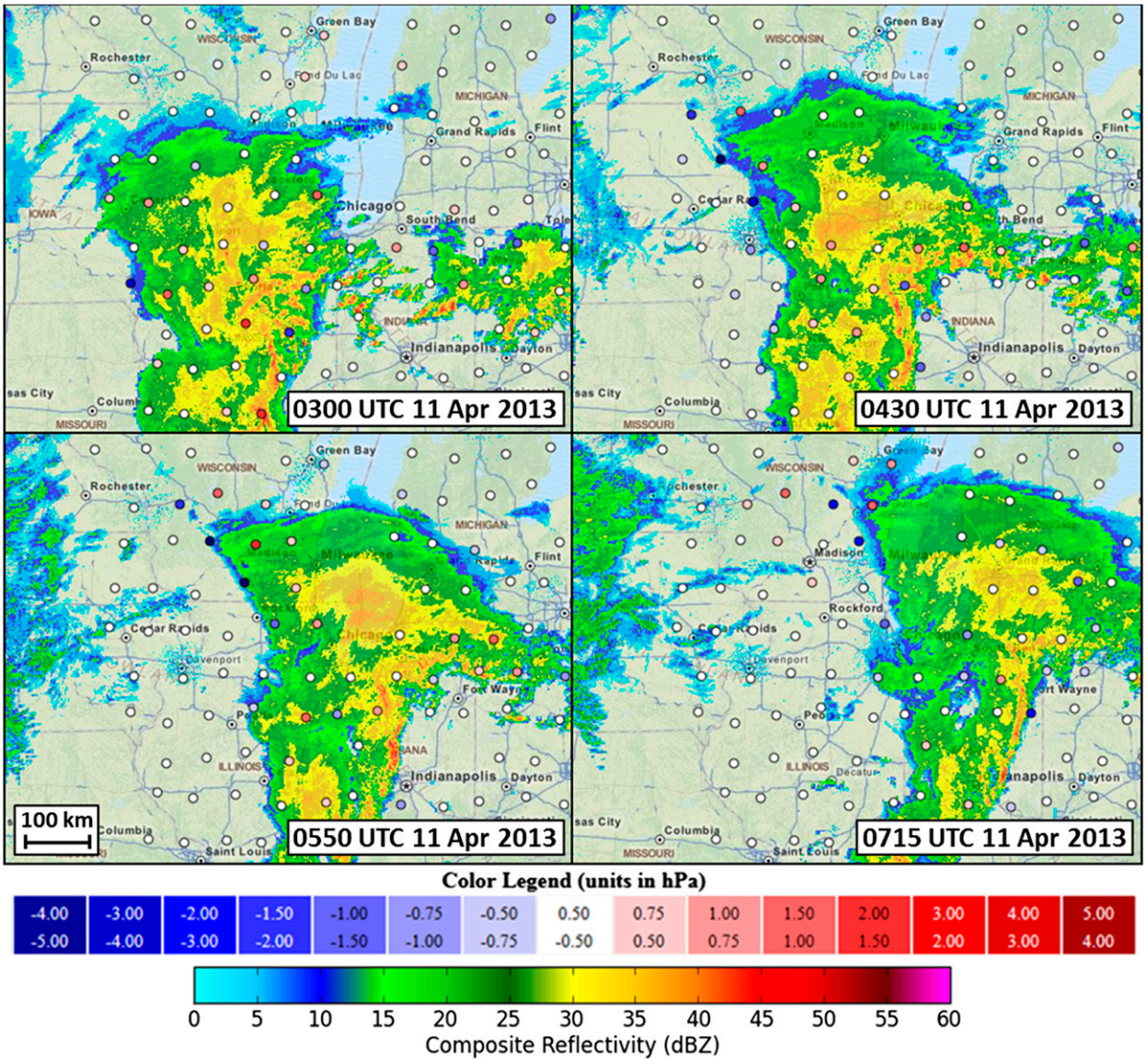

FIG. 7. USArray mesoscale-filtered pressure perturbations (hPa) overlaid on composite radar reflectivity at 0300, 0430, 0550, and 0715 UTC 11 Apr 2013. Red (blue) filled circles indicate positive (negative) perturbations according to the color bar as used on the website (http://meso1.chpc.utah.edu/usarray). Composite radar imagery were provided by the Iowa Environmental Mesonet web services.

control of the 1-Hz data from 1 January 2010 to 28 February 2014. Over 48 billion observations were collected during this time period. Stations had very little missing data with a median loss of only 0.17% of the possible observations per station. The quality control procedures flagged a total of 2.39% of the 1-Hz data, the majority from a few problematic stations or stations that had extended periods of sensor problems that required maintenance. For example, heavy rain events in some instances led to water infiltrating the inlet tubes to the pressure sensors resulting in wild, unphysical swings in pressure. To maintain the integrity of the 1-Hz data archive, suspect data were not removed but simply ignored in subsequent analyses. The available web tools were developed with the ability to view the observed pressure time series with quality control filtering applied or removed, so high-frequency fluctuations labeled as suspect can be assessed visually on a case-by-case basis.

c. *Temporal filtering*

Since very high-frequency ($>1\,\mathrm{min}^{-1}$) perturbations are not of interest in this study and to reduce processing time, 1-min samples were derived from the 1-Hz observations. Three Butterworth bandpass filters (referred

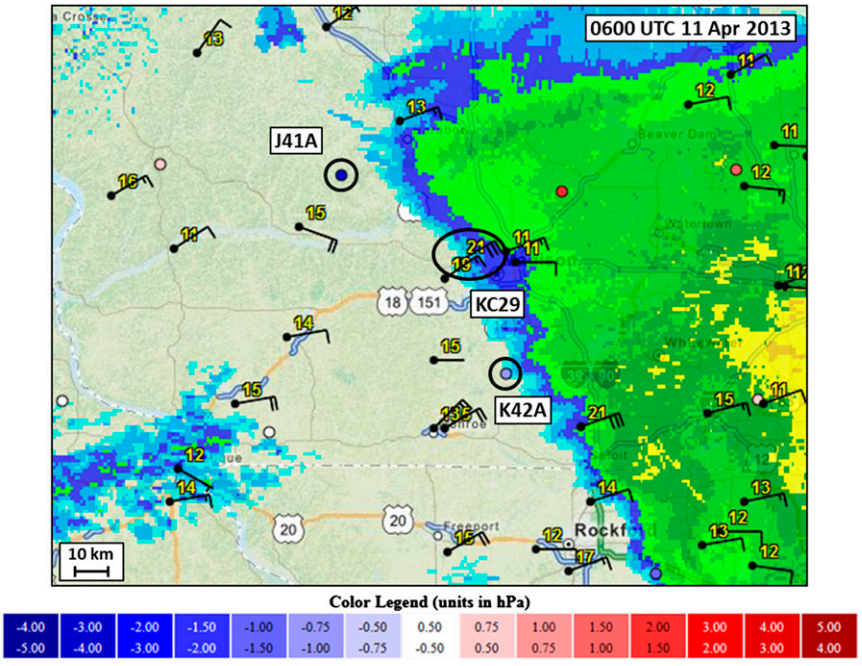

FIG. 8. As in Fig. 7, but near southern Wisconsin at 0600 UTC 11 Apr 2013 with wind observations greater than 10 m s^{-1} added. A full wind barb represents 5 m s^{-1} sustained wind speed, with wind gust values labeled to the top right of the station. Stations discussed in the text are circled and labeled.

to as the meso-, subsynoptic-, and synoptic-scale filters) were applied separately to each 1-min pressure time series after removing the period-of-record mean. These second-order filters using five coefficients were applied twice (forward and backward) to minimize unwanted phase shifts. Figure 3 depicts the squared magnitude response of each bandpass filter versus period. Following the work of Koch and Saleeby (2001), the mesoscale filter attempts to isolate mesoscale pressure perturbations with periods between 10 min and 4 h, which correspond to the micro-α and meso-γ temporal scales according to Orlanski (1975). The synoptic filter (30 h–5 days) was chosen to identify pressure perturbations associated with synoptic-scale weather features. The middle filter (4–30 h) partially overlaps the other two (which introduces some ambiguity when interpreting its specific temporal range) and focuses on pressure perturbations arising from a complex mix of processes including frontal passages (particularly strong cold fronts) and those leading to semidiurnal and diurnal tides. Following Orlanski (1975), this filter encompasses the meso-β temporal scale, and the longer time scales of mesoscale phenomena according to Markowski and Richardson (2010). We are in essence subdividing the total variance of each pressure time series into four bands: mesoscale, subsynoptic, synoptic, and low frequency (i.e., periods longer than 5 days). While the filters are applied continuously to the entire record for each station, the small portions of each time series including and surrounding missing or suspect data are ignored in the subsequent analyses.

Figure 4 illustrates these filtering techniques applied to the 24-h period encompassing the mesoscale gravity wave event shown in Fig. 1. The gravity wave signature near 0600 UTC 11 April 2013 is clearly isolated by the mesoscale filter, while the decreasing pressure trend over the 24-h period is captured by the synoptic filter. The small perturbations on the subsynoptic scale are of less interest in this case. As a contrasting case, Fig. 5 shows pressure traces for a station in southern Texas over a 2-week period during late February 2010. The total range in pressure from +10 to −15 hPa observed during this period is explained in part by perturbations within the synoptic band (±8 hPa) with additional contributions from the subsynoptic band (±3 hPa) and minimal contributions from the mesoscale band. In particular, the subsynoptic band captures the diurnal and semidiurnal fluctuations.

Large pressure rises and falls, hereby denoted as pressure signatures, are identified from each filtered time series. Consecutive local maxima and minima are paired as pressure signature start and end points if they occur within the nominal temporal duration defined for the meso-, subsynoptic-, and synoptic-scale filters (i.e.,

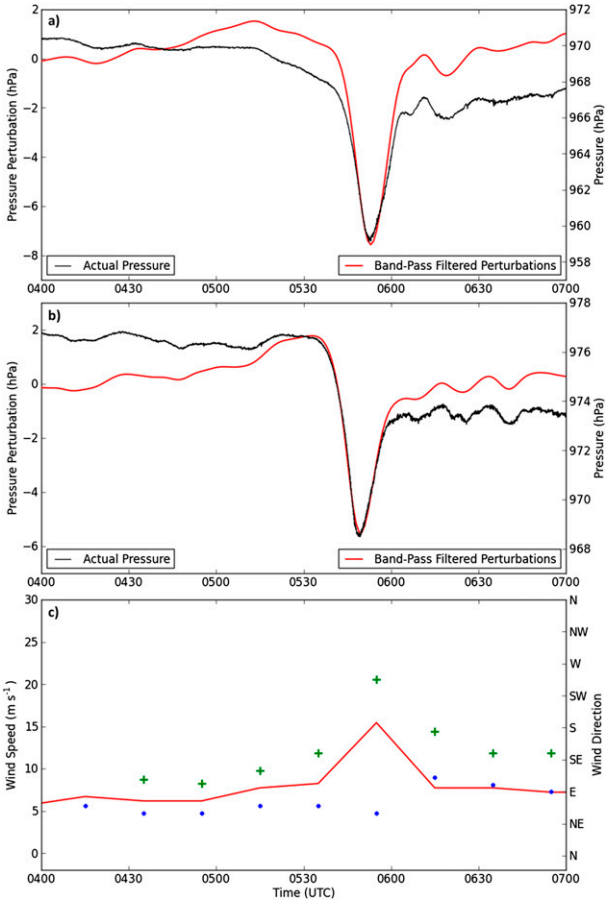

FIG. 9. (a) Time series of 1-Hz pressure (hPa, black line according to scale on the right) and mesoscale bandpass-filtered pressure perturbations (hPa, red line according to scale on the left) for USArray station J41A (Loganville, WI) from 0400 to 0700 UTC 11 Apr 2013. (b) As in (a), but for USArray station K42A (Prairie Point, WI). (c) Wind speed (solid red), wind direction (blue circle markers), and wind gust (green cross markers) for station KC29 (Middleton Municipal Airport, WI).

4 h, 30 h, and 5 days, respectively). Events that occur at the beginning or end of the time series as well as near missing or erroneous data periods were checked manually. Metrics (e.g., duration and absolute and perturbation pressure changes) for each event were calculated and stored for later analysis.

Figure 6 illustrates how the variance in each filtered time series for a particular station and season relates to one another, to the unfiltered variance of the complete time series, and to corresponding variances at other stations. For this particular case, station T37A in southeast Kansas during the 2011 spring (MAM) season, the total variance about the period-of-record mean is 28.2 hPa^2. This value is substantively less than 80 hPa^2, which corresponds to a scaling value defined approximately from the 80th percentile for all unfiltered variance values for all seasons and stations. The variance in the synoptic period (30 h–5 day) is 13.1 hPa^2, which places it approximately near the 40th percentile of all the synoptic-filtered time series (i.e., roughly half of the scaling value of 25 hPa^2 for this band). The large pressure perturbations after 3 May evident in the top time series clearly arise from low-frequency ($<0.2\,day^{-1}$) fluctuations rather than synoptic-scale disturbances that were more common earlier in the spring. The seasonal variances explained by subsynoptic and mesoscale fluctuations during spring 2011 are small (0.82 and 0.058 hPa^2, respectively). However, some large mesoscale events took place and, while small, the variance in the mesoband during this season is greater than the ~80th percentile for all the mesoscale-filtered time series. To allow comparison to other stations during other seasons, the "final marker" in the center right displays the magnitudes of the four variance values as vectors in specified compass directions. Interpretation of the marker relative to the 80th percentile scaling vectors indicates that the unfiltered, synoptic, and subsynoptic variances at this station for spring 2011 were below average to average compared to other stations during all seasons, but the mesoscale variance was quite large, indicating active mesoscale phenomena at this station during this season.

3. Case studies

a. *Overview*

The web-based products (http://meso1.chpc.utah.edu/usarray/) developed as part of this study to visualize the USArray TA data allow detailed examination of thousands of pressure signatures arising from a wide variety of weather phenomena. For this study, three examples were selected to highlight these analysis capabilities that include relating the available USArray TA pressure observations to surface wind observations and conventional radar imagery. Two events with prominent mesoscale perturbations and one synoptic-scale event were selected to illustrate meteorological features that are commonly studied. As described in section 2, the pressure time series in Fig. 5 illustrates subsynoptic-scale forcing resulting from diurnal and semidiurnal tides.

b. *11 April 2013 Midwest gravity wave event*

One of the stronger mesoscale pressure signatures found in this study was a solitary wave of depression on 11 April 2013 (Figs. 1 and 4). A strengthening synoptic storm system over the central United States produced several rounds of convection and mesoscale gravity waves from 10–11 April 2013 over a large swath of the country, stretching from the Gulf of Mexico through the

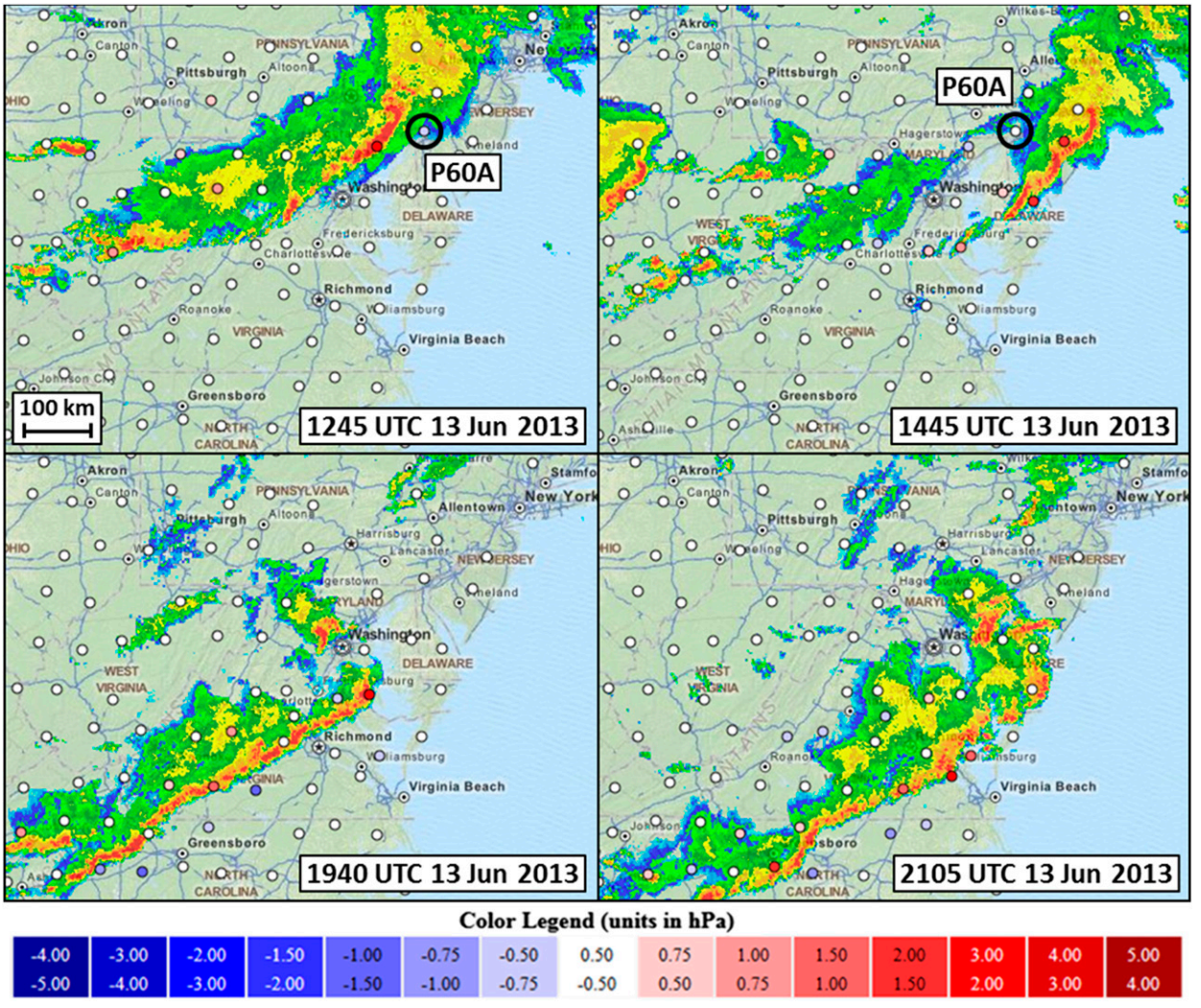

FIG. 10. As in Fig. 7, but for two derecho events across the mid-Atlantic at 1245, 1445, 1940, and 2105 UTC 13 Jun 2013.

Great Lakes region. Similar to the 7 March 2008 solitary wave of depression studied by Ruppert and Bosart (2014), Fig. 7 depicts the wave propagation from Iowa into Wisconsin. Circled markers show the locations of the USArray stations, with the marker color denoting the value of the mesoscale-filtered pressure perturbation at the selected time. Large negative pressure perturbations trail the northern edge of the precipitation complex from Iowa into Wisconsin, which is evident in the radar imagery provided courtesy of the Iowa Environmental Mesonet. Such large negative pressure perturbations are a common signature seen in many solitary mesoscale gravity wave structures with precipitation (Ramamurthy et al. 1993). According to Ruppert and Bosart (2014), precipitation regions such as the region depicted here also may contribute to the large pressure reduction seen directly behind the precipitation shield, and often these systems can further evolve into mesohigh–wake low couplets.

Figure 8 focuses on the region near J41A (Figs. 1 and 4) at approximately the time of the wave's peak intensity

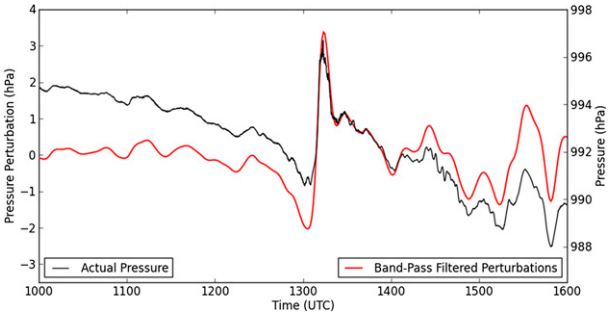

FIG. 11. As in Fig. 9a, but for station P60A (Greenville, DE) from 1000 to 1600 UTC 13 Jun 2013.

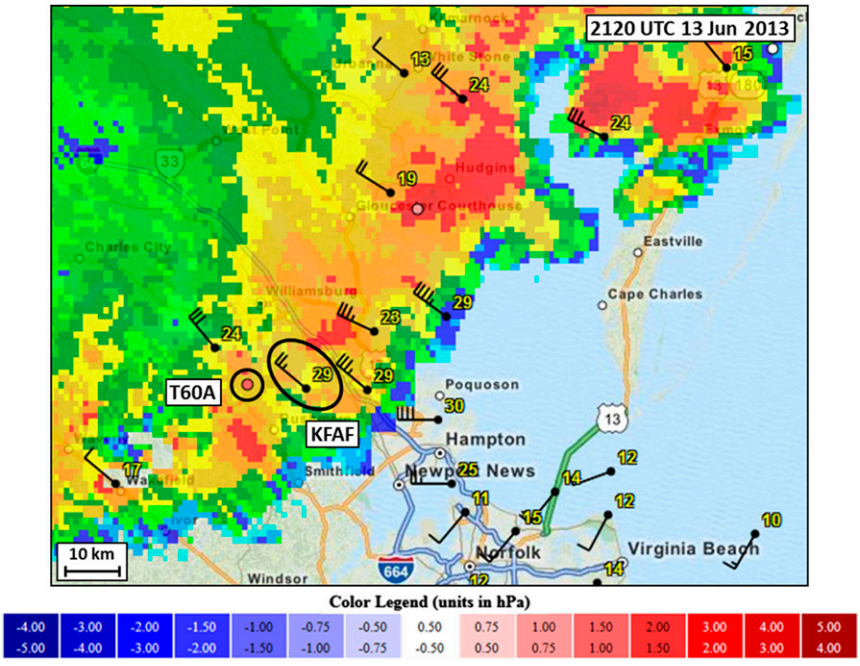

FIG. 12. As in Fig. 8, but for the derecho event across the mid-Atlantic at 2120 UTC 13 Jun 2013.

(0600 UTC) over southern Wisconsin. Included are surface wind observations with reported sustained or gust values larger than 10 m s^{-1}. Stations with the largest sustained winds and gusts were collocated with the back edge of the precipitation. Time series of the mesoscale-filtered pressure data for USArray station J41A and K42A (Fig. 9) depict mesoscale pressure drops of 9.1 hPa in 40 min and 7.3 hPa in 17 min preceded by negligible or small 0.5-hPa pressure rises, respectively. Wind observations at Middleton Municipal Airport (KC29, Fig. 9c) are predominantly from the east-northeast at 5–8 m s^{-1} preceding the event. Sustained wind speeds increase to ~15 m s^{-1} with gusts over 20 m s^{-1} during the wave passage and then lessen during the next hour as the wave propagates eastward.

c. 13 June 2013 mid-Atlantic derecho

Thunderstorms associated with a shortwave trough over the Great Lake region late on 12 June 2013 led to the eventual development of two long-lived MCS/derecho events that produced widespread wind damage from the Ohio Valley eastward. Both events meet the definition of a derecho as described by Johns and Hirt (1987), and the secondary complex was described as a weak derecho by the Blacksburg, Virginia, NWS office as a result of its continuity (wind damage extending greater than about 400 km) and extensive number of severe (25.9 m s^{-1} or greater) straight-line wind damage reports along the damage swath (National Weather Service Weather Forecast Office 2014).

The first complex formed over northern Indiana and Ohio early on 13 June 2013 and moved east-southeast through the mid-Atlantic region and eventually off the coast by 1600 UTC. A second convective complex formed over central Indiana at ~1000 UTC and

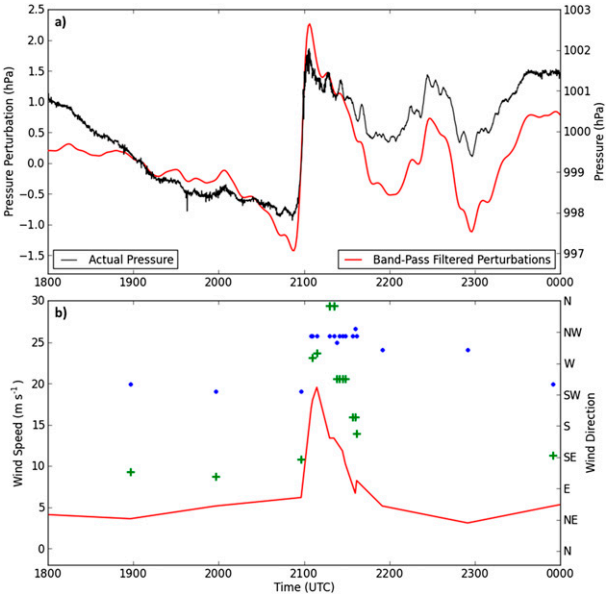

FIG. 13. (a) As in Fig. 9a, but for USArray station T60A (Surry, VA) from 1800 UTC 13 Jun to 0000 UTC 14 Jun 2013 during a derecho event. (b) As in Fig. 9c, but for station KFAF (Felker Army Airfield, VA) between 1800 UTC 13 Jun and 0000 UTC 14 Jun 2013.

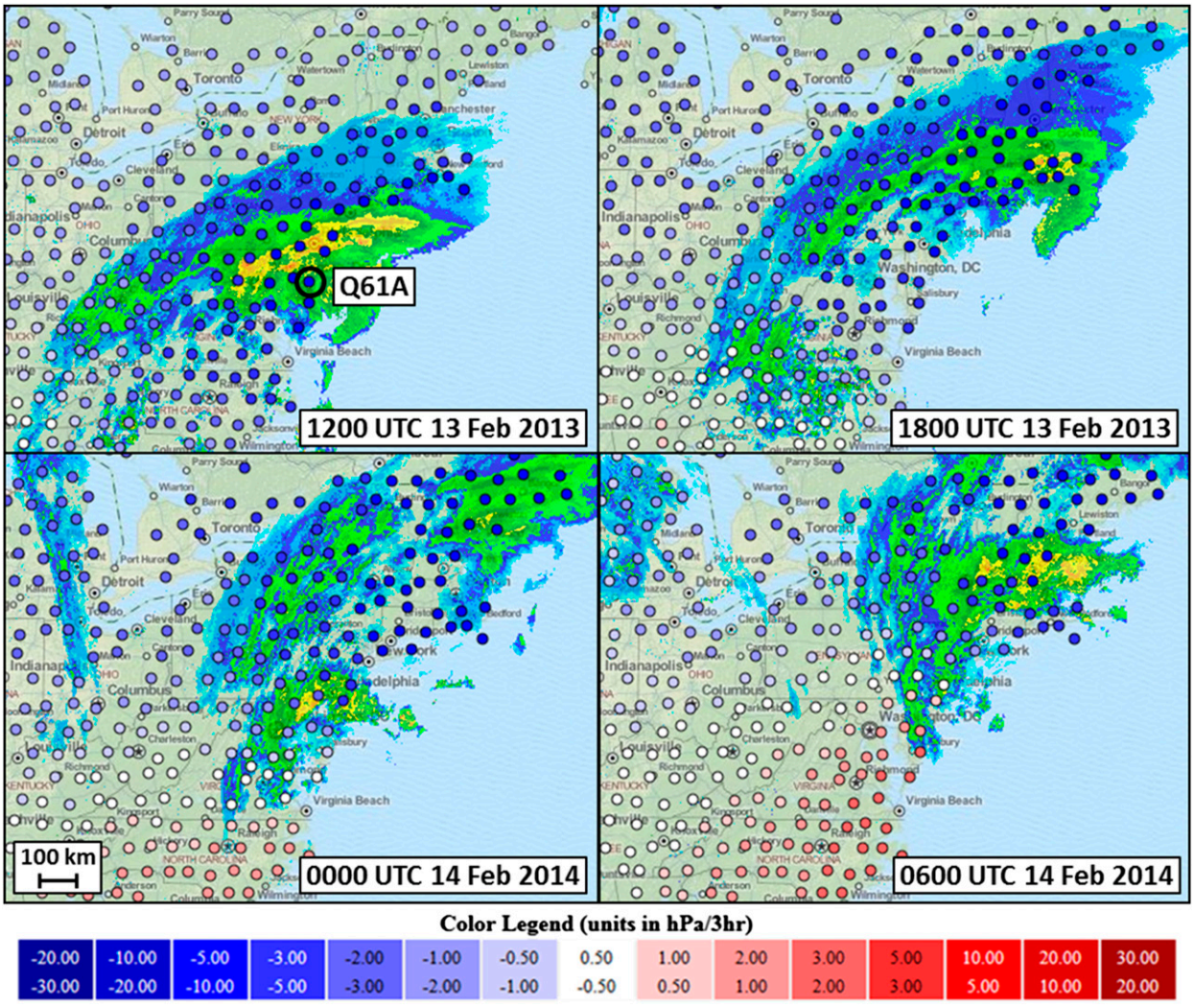

FIG. 14. USArray synoptic-filtered pressure tendency (hPa $3\,h^{-1}$) overlaid with radar reflectivity imagery for a northeast snowstorm event from 1200 UTC 13 Feb to 0600 UTC 14 Feb 2014. Red (blue) filled circles indicate positive (negative) pressure tendencies according to the color bar as used on the website (http://meso1.chpc.utah.edu/usarray).

propagated through Ohio, Kentucky, West Virginia, Virginia, and North Carolina through the remainder of the day. The first complex had a more classic bow-echo structure, with convective cells along a bowed singular line. The second system was more complex with several small clusters of convection developing into a larger squall line late in the duration of the event. The top panels of Fig. 10 show the propagation of the first complex off the coast from 1245 to 1445 UTC, while the second complex is displayed in the bottom panels from 1940 to 2105 UTC. Both events produce large positive perturbations at USArray stations at the leading edge of the convection.

The largest mesoscale pressure rise associated with these two complexes occurred at station P60A in northern Delaware (Fig. 11). A 5.4-hPa rise in 11 min was calculated from the mesoscale-filtered data, which equates to a 29.56 hPa h^{-1} rate of change. However, surface observations near the station did not record any severe wind gusts. The second complex produced numerous severe wind observations as it reached the southern Virginia coastline as seen in Fig. 12. Pressure and wind time series for USArray station T60A and Felker Army Field (KFAF) are shown in Figs. 13a and 13b, respectively. Station T60A had a 3.7-hPa increase in 11 min, while nearby station KFAF recorded wind gusts near 30 m s^{-1} immediately after the passage of the primary gust front. Comparing the pressure time series evolution between USArray station P60A (Fig. 11) and T60A (Fig. 13) provides insight into the derecho

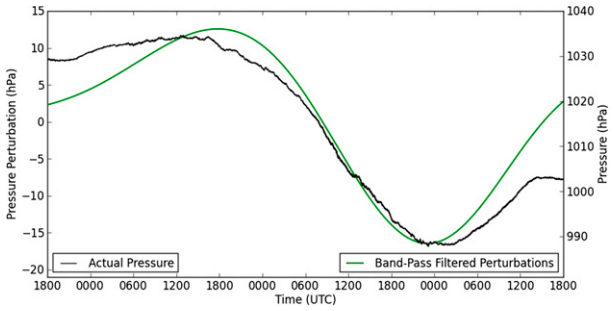

FIG. 15. Time series of 1-Hz pressure (hPa, black line according to scale on the right) and synoptic bandpass-filtered pressure perturbations (hPa, green line according to scale on the left) for USArray station Q61A (Milford, DE) from 1800 UTC 11 Feb to 1800 UTC 14 Feb 2014.

evolution and spatial variability that would not be seen using filtered or averaged pressure data. At P60A, the 5.4-hPa pressure rise was immediately followed by a several hectopascal pressure drop 10 min later, with several hours of more gradual pressure falls thereafter (Fig. 11). However, at T60A, the strengthening of the cold pool behind the derecho resulted in a more prolonged pressure maximum (~30 min) and a reduced pressure fall (with a secondary pressure rise behind the derecho likely associated with outflow).

d. 2014 Valentine's Day Storm

A strong synoptic system, originating in the Gulf of Mexico, moved up the East Coast of the United States during 13–15 February 2014. The storm brought widespread heavy snowfall for inland regions spanning from northwestern North Carolina through Maine. Figure 14 shows the evolution of this event as an area of low pressure developed off the mid-Atlantic coastline, strengthened, and moved northeast toward Nova Scotia. The shading of the USArray stations is derived from a 3-h pressure tendency based on the synoptic-filtered dataset to lessen the impact of other time scales in the unfiltered data. The dark blue circles indicated large pressure falls on the synoptic scale, which were located ahead of the propagating synoptic wave. The largest

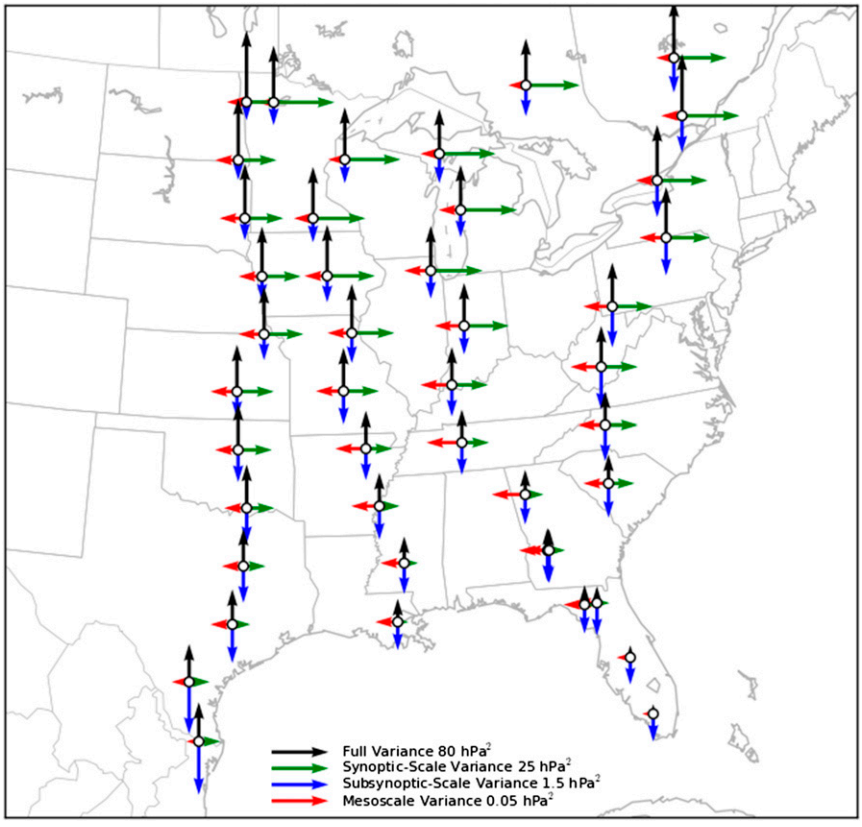

FIG. 16. USArray pressure perturbation variance during winter (DJF) seasons from 2010–11 to 2013–14. The variance values at each station are combined into station clusters as described in the text. See Fig. 6 for the description of the markers with vector scaling lengths provided at the bottom.

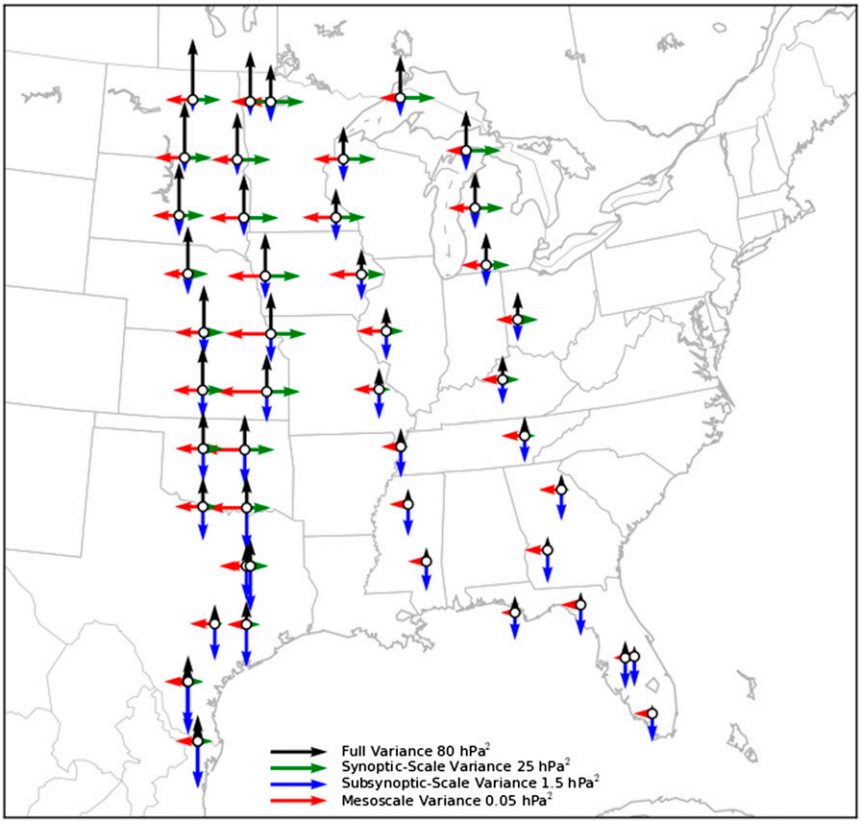

FIG. 17. As in Fig. 16, but for spring (MAM) seasons during 2010–13.

falls were located across New England during 0000–0600 UTC 14 February 2014. Behind the system, pressure rises are seen, with the largest values located along the coastline closest to the low pressure. The unfiltered and synoptic-filtered time series for station Q61A in Delaware are shown in Fig. 15. Whether evaluated on the basis of the unfiltered or synoptic-filtered data, the pressure falls of 40 hPa or 29 hPa, respectively, in 29 h are impressive.

4. Perturbation pressure variance

To summarize seasonal and spatial differences in the amplitude of the pressure perturbations, the variance vectors introduced in Fig. 6 are now used as shown in Figs. 16–19. Referring to Fig. 2, station clusters are used to reduce the number of vectors displayed on the figures as well as account for the eastward progression of the array during the four years of this study (i.e., there are four roughly north–south-oriented lines of clusters available for each calendar season). Each cluster comprises 2–50 (median 23) stations within 2° × 6° latitude–longitude bins during each season. The vectors shown in these figures represent the median variance values derived from the sample of time series available within each cluster.

During the winter (DJF) months (Fig. 16), the unfiltered (black vector pointing north) and synoptic-filtered (green vector pointing east) variance increases with latitude. When the array was located farthest west during the 2010–11 winter and along the East Coast during the 2013–14 winter, the unfiltered variance tended to be larger in the northern tier of clusters than during the 2011–12 and 2012–13 winters. Less longitudinal and interannual variance is evident in the synoptic-filtered data. A tendency for subsynoptic variance (blue vectors pointing south) to decrease with latitude is apparent, particularly during the 2010–11 winter with high subsynoptic variance evident in southern Texas. Mesoscale variance (red vectors pointing west) is largest in the center of the USArray during the 2011–12 and 2012–13 winters.

During the spring (MAM) months (Fig. 17), unfiltered and synoptic variances are reduced from those found during winter (Fig. 16), except for the 2010 and 2011 spring seasons over the upper Great Plains. The largest subsynoptic variance remains over Texas. Substantively

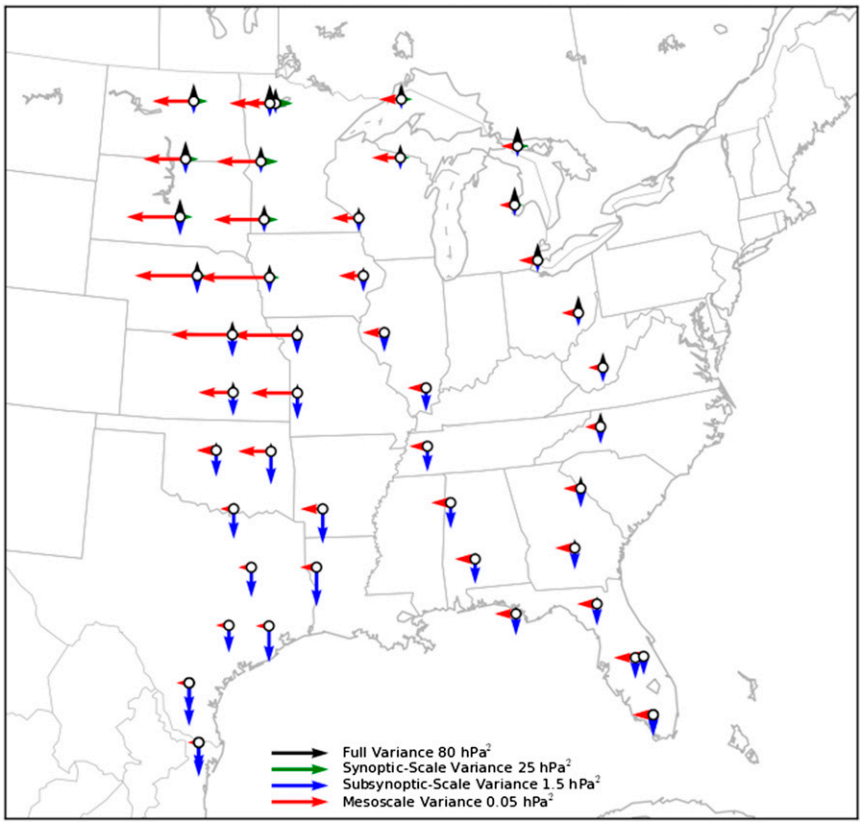

FIG. 18. As in Fig. 16, but for summer (JJA) seasons during 2010–13.

larger mesoscale variance during the 2011 spring season is evident from Oklahoma northward to Iowa.

As shown in Fig. 18, the unfiltered and synoptic variances reach their minimum values during summer (JJA) compared to other seasons. Large mesoscale variance is evident over the central Great Plains during the 2010 and 2011 summers. The subsynoptic variance is lower during the summer months across the southern United States compared to that during spring.

The latitudinal increase in the unfiltered and synoptic variance evident during winter appears as well during autumn (SON) months (Fig. 19), particularly during the 2013 autumn with high values over southeast Canada. Large subsynoptic variance is evident again over southern Texas during the 2010 autumn. Mesoscale variance values are small overall compared to other seasons.

5. Pressure signatures

Figures 20 and 21 summarize pressure signatures derived from the synoptic bandpass-filtered data. As introduced in section 2c, event start and end points are defined by consecutive local maxima and minima in a filtered time series if they occur within the nominal maximum temporal duration defined for the synoptic, subsynoptic, and mesoscale filters (i.e., 5 days, 30 h, and 4 h, respectively). The difference between the maximum and minimum pressure divided by the time interval between the start and end times defines the pressure rate of change. Using the case presented in Fig. 15 as an illustration, the 29.2-hPa pressure fall over 29.4 h corresponds to a rate of $-23.9\,\text{hPa day}^{-1}$, while the subsequent pressure rise of 21.7 hPa over 25.3 h leads to a $20.6\,\text{hPa day}^{-1}$ rate. Hence, two pressure signatures often result from a single weather disturbance passing over a station.

A total of 62 482 synoptic signatures were discovered to have a pressure rate of change larger than $8\,\text{hPa day}^{-1}$, with 74.5% of signatures having a temporal duration between 22 and 36 h (Fig. 20a). Large synoptic pressure signatures are defined here as having pressure rates exceeding $18\,\text{hPa day}^{-1}$, approximately the 95th percentile of all synoptic signatures. This threshold also falls within limits of other similar thresholds between 16 and $25\,\text{hPa day}^{-1}$ (Alexandersson et al. 1998; Bärring and Fortuniak 2009; Krueger and von Storch 2012).

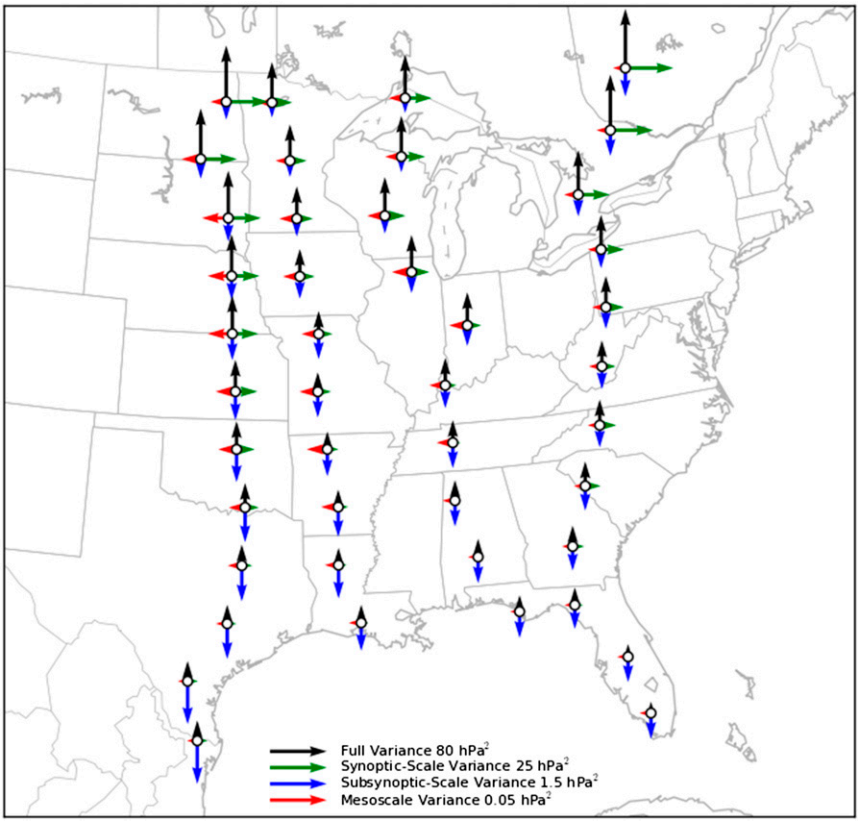

FIG. 19. As in Fig. 16, but for autumn (SON) seasons during 2010–13.

Figure 20b indicates that very few large synoptic signatures had temporal durations longer than 36 h (1.2%), indicating that stronger signatures were associated with shorter-duration synoptic events.

Using the 18 hPa day^{-1} threshold, a total of 3269 large synoptic pressure signatures were detected during the 4-yr period. Synoptic pressure signatures are most frequent during the winter months (Fig. 21a). Maximum values of ~20 synoptic large pressure signatures per season occurred during the 2014 winter along the northeast coast of the United States corresponding roughly to ~10 strong weather disturbances during that winter. A secondary maximum is evident over the northern Great Plains during the 2011 and 2012 winters. The frequency of such large pressure signatures drops substantively during spring (Fig. 21b) with only a few evident across the northern tier of reporting stations. Very few such synoptic signatures were seen during the summer months [e.g., the landfall of Hurricane Isaac contributed to a 23.9-hPa drop in 27 h near Chauvin, Louisiana (station 645A), in the synoptic filtered data]. During autumn, an increase toward the northeast is evident, in particular for the stations over southern Ontario and Quebec provinces (Fig. 21d).

The ubiquitous occurrence during all seasons of modest subsynoptic-scale pressure fluctuations is evident in Figs. 22 and 23. Using an initial 0.5-hPa pressure change threshold, 1 187 795 subsynoptic signatures

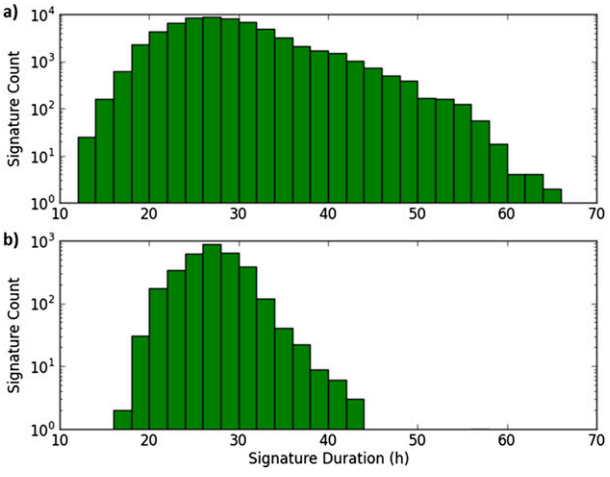

FIG. 20. (a) Synoptic pressure signature frequencies as a function of signature temporal duration (h) for all signatures detected (pressure rate magnitude exceeding 8.0 hPa day^{-1}). (b) As in (a), but for only large signatures (pressure rate magnitude exceeding 18.0 hPa day^{-1}). Signature count axis is given in log scale.

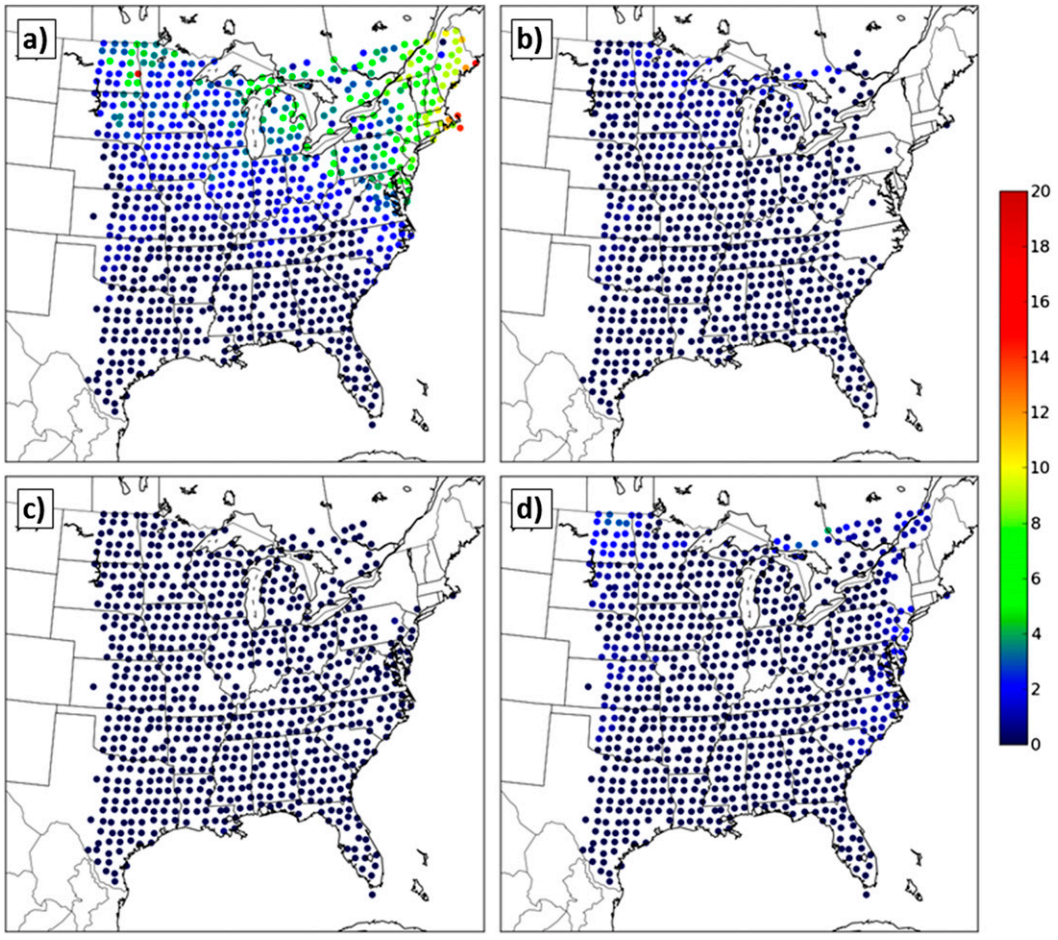

FIG. 21. Synoptic pressure signatures per season with pressure rate magnitudes exceeding 18.0 hPa day^{-1} according to the scale on the right during (a) winter (DJF), (b) spring (MAM), (c) summer (JJA), and (d) autumn (SON).

were discovered with a wide range of temporal durations (Fig. 22a). As shown in Fig. 5, many of these signatures appeared to be associated with fluctuations due to the superposition of diurnal and semidiurnal tides. Large-magnitude subsynoptic signatures are defined here by a pressure rate of change exceeding 1 hPa h^{-1}. This threshold effectively removes routine diurnal and semidiurnal pressure fluctuations, while retaining strong signatures associated with cold frontal passages and larger convective complexes. A total of 5262 large subsynoptic pressure signatures were found during the 4-yr period, with temporal durations primarily between 3 and 8 h. Figure 23 shows that a peak of ~10 signatures occurred each season during winter, spring, and summer, with a minimum number occurring during the fall. The maxima during winter occur in the Ohio Valley into the northeastern United States while the peak number of signatures occur in the central Great Plains region during spring and summer.

From the mesoscale-filtered time series, 301 294 signatures were found using an initial absolute pressure change greater than 1 hPa within 4 h. The majority of these signatures (82.7%) occurred within 1 h (Fig. 24a). Large pressure signatures are defined as those having an absolute pressure change greater than 3 hPa within 4 h, corresponding to the 95th percentile of all mesoscale pressure signatures computed. A total of 15 703 mesoscale pressure signatures were found during the 4-yr sample, again with the majority (83.2%) within 1 h (Fig. 24b). As shown in Fig. 25, very few occurred during autumn and winter. During the 2010–13 spring seasons, large pressure signatures were more commonplace over the central plains and upper Midwest regions, with 20–25 signatures per season evident from Oklahoma northwestward toward Wisconsin. A secondary smaller maximum is also

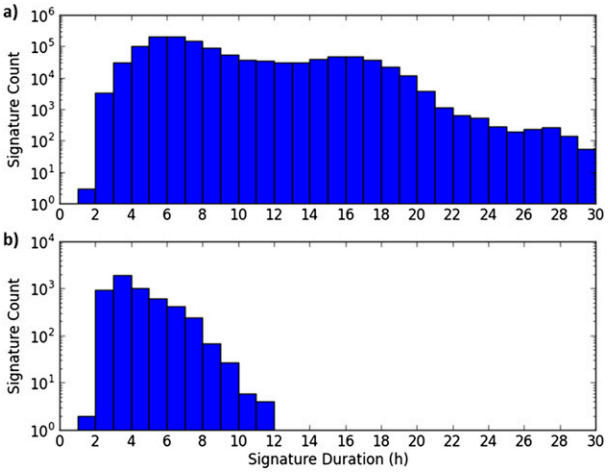

FIG. 22. (a) Subsynoptic pressure signature frequencies as a function of signature temporal duration (h) for all signatures detected (pressure change magnitude exceeding 0.5 hPa). (b) As in (a), but for only large signatures (pressure rate magnitude exceeding 1.0 hPa h^{-1}).

evident in the southeast over Georgia during spring. A pronounced maximum in mesoscale pressure signatures is evident over the states of Nebraska and Iowa during summer. Several stations recorded 35–40 pressure signatures per season from the 2010–12 summers when the array was located in this region.

6. Summary and discussion

Surface pressure observations from the USArray have been examined at meso- (10 min–4 h), subsynoptic (4 h–30 h), and synoptic (30 h–5 days) scales. This study is the first to look at the variance of pressure signatures on multiple temporal scales over a broad region at relatively uniform spacing. A unique data source of 1-Hz sampled pressure observations from the eastward-propagating USArray seismic project network was used for this study. Bandpass filters at mesoscale, subsynoptic, and synoptic frequencies were applied to the pressure time series and the occurrences of large-magnitude pressure signatures were identified objectively. All of the resulting tens of thousands of pressure signature events can be looked at individually or collectively through a web interface (http://meso1.chpc.utah.edu/usarray). Several representative case studies were examined here in section 3 followed by aggregate statistics in sections 4 and 5. The high temporal resolution of the USArray pressure data provides an enhanced perspective relative to other conventional sources of pressure data for studying mesoscale phenomena, some of which exhibit sharp short-duration pressure perturbations that can propagate over hundreds of kilometers. It is not our intention to imply that the USArray provides a great deal of added value for studying longer-duration pressure perturbations compared to hourly pressure reports available from other meteorological networks. However, there is considerable value in contrasting the characteristics of pressure perturbations over a range of temporal scales using a consistent dataset as is done in this study.

The relatively short deployment (~2 yr) for each pressure sensor limits interpreting the results of this study as a long-term climatology of pressure perturbations and signatures for a specific locale, although gravity wave climatologies were estimated using even shorter records by Einaudi et al. (1989) and Lee and Barr (1998). This shortcoming is compensated for in some respects by the rich detail afforded by the high temporal sampling. For example, the long-term climatology of mesoscale pressure signatures by Koppel et al. (2000) based on hourly pressure changes larger than 4.25 hPa misses, not surprisingly, the majority of mesoscale pressure signatures (Fig. 24). In addition, we have taken care to compensate as best as possible for the year-to-year variability in pressure perturbations by grouping stations as a function of their deployment (Figs. 16–19). Hence, the larger synoptic variance evident in Fig. 16 in the northeastern United States and southern Canada during the 2013–14 winter compared to the smaller synoptic variance in the Great Lakes region during the previous two winters is likely due to year-to-year variations in storm tracks embedded within the planetary-scale circulation.

The cumulative statistics presented in sections 4 and 5 help to delineate several obvious patterns associated with weather features that are accompanied by pressure perturbations on time scales from minutes to seasons. Foremost, as with nearly all geophysical phenomena, the magnitude of the variance of pressure perturbations at low frequencies (spanning beyond 5 days) is larger than that for any of the filtered bands (synoptic, subsynoptic, or mesoscale) and the variance within the mesoscale band is the weakest of all. Hence, while the pressure signatures associated with mesoscale severe weather events tend to be quite distinct and frequent (Fig. 22), their relative amplitude during all seasons is small compared to the pressure changes associated with more benign shifts in the large-scale circulation (note the relative scales in Figs. 16–19). During winter and fall, the pressure perturbations are most dominated by low-frequency (longer than 5 days) and synoptic-scale fluctuations (Figs. 16 and 19) with increasing synoptic variance with increasing latitude.

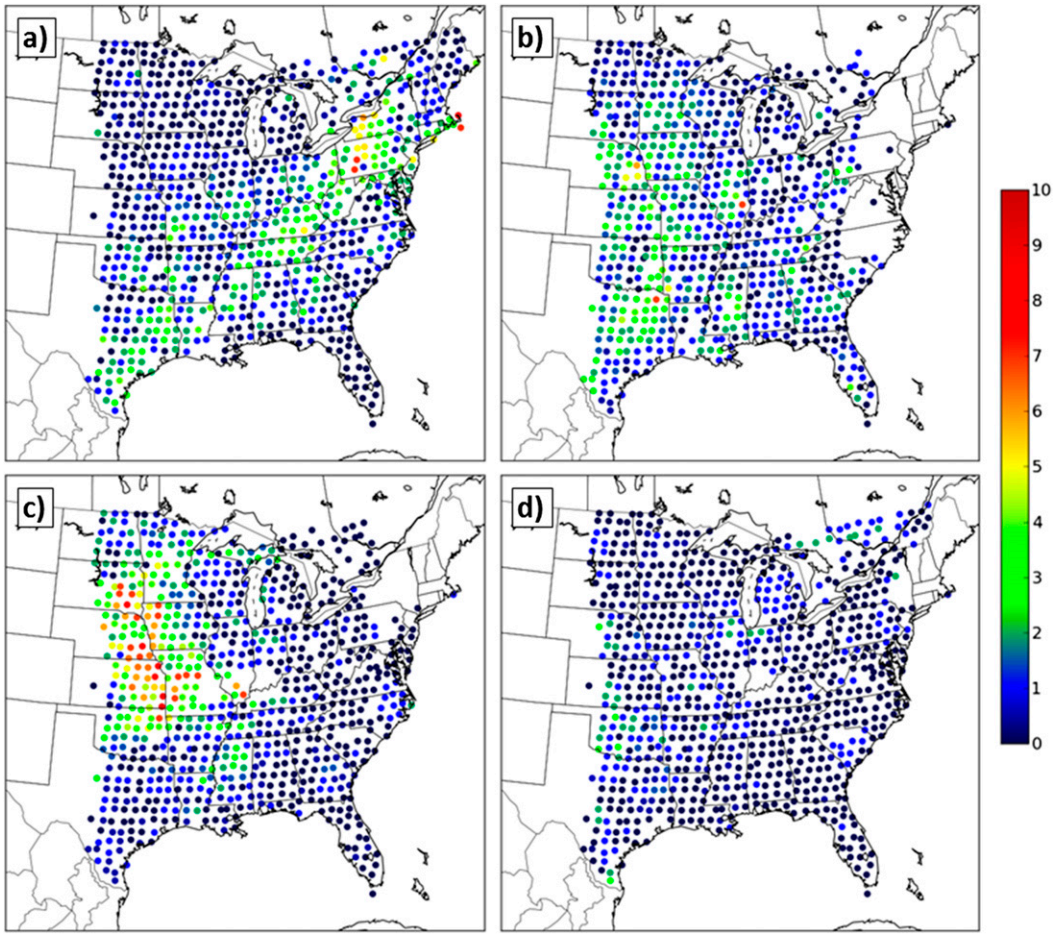

FIG. 23. As in Fig. 21, but for subsynoptic pressure signatures with pressure rate magnitudes exceeding 1 hPa h^{-1}.

Phenomena on subsynoptic scales and mesoscales tend to be more ubiquitous during the warm seasons with mesoscale events prominent during the 2010 and 2011 spring and summer seasons over the central Great Plains (Figs. 23 and 25). Climatologically, severe convective events begin to peak in frequency across the southern plains during the spring, suggesting the large pressure signature maxima over Oklahoma and Arkansas in Fig. 17 that shift northward to the central Great Plains during summer in Fig. 18 are likely due to organized convective activity. The seasonal variations of the large-magnitude subsynoptic pressure signatures evident in Fig. 23 highlight the diversity of mechanisms capable of forcing them [e.g., sharp frontal passages during the winter and mesohighs, wake lows, and sequences of organized convection during summer; Carbone et al. (2002)]. Pressure variations in the southern half of the United States exhibit pronounced diurnal and semidiurnal cycles in pressure during summer (Fig. 18). As the USArray shifted east during the 2012 and 2013 warm seasons, the number of large mesoscale pressure perturbations diminished because of reduced convective activity (Figs. 23 and 25).

The over 48 billion pressure observations collected by the USArray TA pressure network and analyzed here are available for statistical analysis and graphical display (http://meso1.chpc.utah.edu/usarray/). While the period of this study ended on 28 February 2014, USArray TA pressure data are still being collected routinely and available via the web. Approximately 180 stations are being left in place to collect data for several years across the eastern and central United States. As part of the EarthScope initiative, another subset of the USArray is to be deployed across Alaska beginning in late 2014.

This study introduces the USArray TA pressure data in part as a means to stimulate further research whether at specific locales [e.g., Lee and Barr (1998)

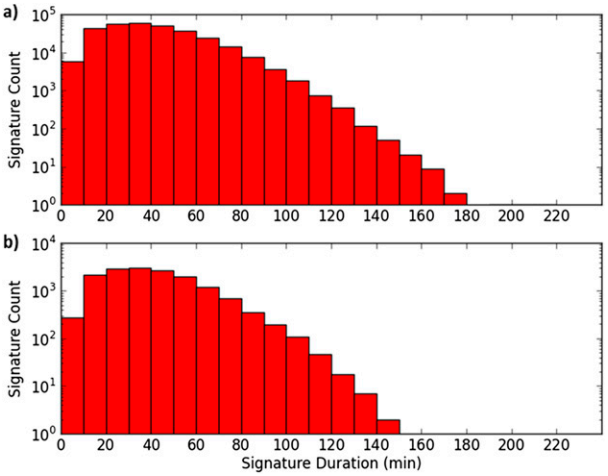

FIG. 24. (a) Mesoscale pressure signature frequencies as a function of signature temporal duration (min) for all signatures detected (pressure change magnitude exceeding 1 hPa). (b) As in (a), but for only large signatures (pressure change magnitude exceeding 3 hPa).

analyzed gravity waves within a forest] or simultaneously tracking multiple medium to large-amplitude pressure signatures and their spatiotemporal interactions (e.g., Adams-Selin and Johnson 2010). The broad geographic coverage at ~70-km horizontal resolution afforded by the pseudogridded USArray TA over the eastern United States during the 2010–14 period provides an excellent dataset for case-study analysis of large-amplitude gravity wave propagation dynamics within this region. These large-amplitude gravity waves (both solitary and wave packets) are known to propagate several hundred kilometers at speeds of 10–35 m s^{-1} (Adams-Selin and Johnson 2010; Ruppert and Bosart 2014; Clark et al. 2014), which extends beyond the geographic range of previous moderate-density pressure networks that have been used to study large-amplitude gravity waves (e.g., Koch and Siedlarz 1999; Jewett et al. 2003).

The capability for researchers to examine individual as well as sets of large pressure perturbations within temporal bands (meso-, subsynoptic, and synoptic scales) or simply from the unfiltered pressure time series is an important outcome of this study. Since the temporal evolution of some weather events does not fit neatly into the filter windows selected here (e.g., the multiple convective events described by Carbone et al. 2002), careful evaluation of the unfiltered and filtered data is necessary as well as taking advantage of other data resources. For example, vertical rawinsonde profiles at Green Bay, Wisconsin, and Davenport, Idaho, confirm that the environmental conditions favorable for forming and maintaining ducted gravity waves (e.g., shallow surface mixed layer capped by a strong stable layer and wind reversal with height) were present during the 11 April 2013 gravity wave case discussed in section 3b (not shown).

Researchers may find the pressure data useful for validating forecasts available from research and operational numerical weather prediction models. For example, forecasts at lead times of 1–2 days from the Global Forecast System model of the National Centers for Environmental Prediction (NCEP) suggested internal gravity waves were likely to form within an evolving northeast United States coastal low on 26 November 2014 (not shown). Researchers following this event used the USArray pressure website to evaluate the model guidance and to interpret the subsequent development of banded precipitation features within the storm evident in radar imagery (B. Colle 2014, personal communication).

To develop high-resolution gridded fields of sea level pressure over the USArray domain, we are now testing a two-dimensional variational analysis technique to create sea level pressure grids at 2.5-km horizontal resolution at 5-min intervals. These grids are being used to examine the propagation of mesoscale pressure perturbations that are difficult to detect from the widely spaced USArray alone or from other conventional meteorological networks. Surface pressure 1-h forecasts available every hour from the NCEP Rapid Refresh model are downscaled by NCEP to a 2.5-km grid for the Real-Time Mesoscale Analysis (RTMA; de Pondeca et al. 2011). We interpolate the differences in these pressure fields from one hour to the next using cubic splines in the time domain at 5-min intervals. The corresponding 1-h differences in pressure at the USArray locations are then used to adjust the background fields using the variational approach described by Tyndall and Horel (2013). Applying this approach to the 11 April 2013 case examined in section 3b demonstrates the spatial and temporal continuity of the wave progressing across the Great Lakes region.

Acknowledgments. Funding for this research was provided by National Science Foundation Grant 1252315. Access to USArray pressure data was provided by the Incorporated Research Institutions of Seismology Web Services, as well as the Array Network Facility at Scripps Institution of Oceanography, University of California, San Diego. Web product radar imagery was courtesy of the Iowa Environmental Mesonet web services. Wind observations were provided by developmental API services courtesy of MesoWest. The authors thank the University of Utah Center for High

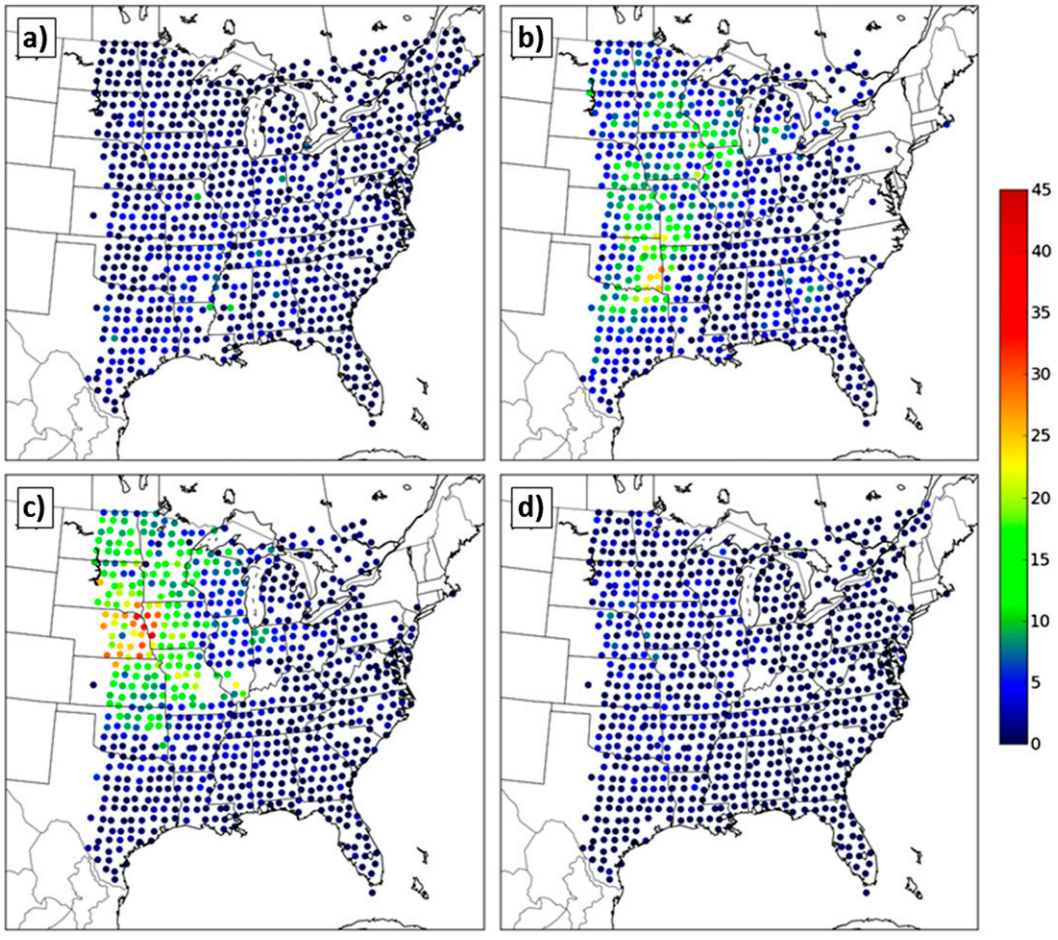

FIG. 25. As in Fig. 21, but for mesoscale pressure signatures with pressure change magnitudes exceeding 3 hPa.

Performance Computing (CHPC) for computational hardware and software, as well as providing a host location for developed web products.

REFERENCES

Adams-Selin, R. D., and R. H. Johnson, 2010: Mesoscale surface pressure and temperature features associated with bow echoes. *Mon. Wea. Rev.,* **138,** 212–227, doi:10.1175/2009MWR2892.1.

——, and ——, 2013: Examination of gravity waves associated with the 13 March 2003 bow echo. *Mon. Wea. Rev.,* **141,** 3735–3756, doi:10.1175/MWR-D-12-00343.1.

Alexandersson, H., T. Schmith, K. Iden, and H. Tuomenvirta, 1998: Long-term variations of the storm climate over NW Europe. *Global Atmos. Ocean Syst.,* **6,** 97–120.

Bärring, L., and K. Fortuniak, 2009: Multi-indices analysis of southern Scandinavian storminess 1780–2005 and links to interdecadal variations in the NW Europe-North Sea region. *Int. J. Climatol.,* **29,** 373–384, doi:10.1002/joc.1842.

Bosart, L. F., W. E. Bracken, and A. Seimon, 1998: A study of cyclone mesoscale structure with emphasis on a large-amplitude inertia–gravity wave. *Mon. Wea. Rev.,* **126,** 1497–1527, doi:10.1175/1520-0493(1998)126<1497:ASOCMS>2.0.CO;2.

Carbone, R. E., J. D. Tuttle, D. A. Ahijevych, and S. B. Trier, 2002: Inferences of predictability associated with warm season precipitation episodes. *J. Atmos. Sci.,* **59,** 2033–2056, doi:10.1175/1520-0469(2002)059<2033:IOPAWW>2.0.CO;2.

Clark, P. A., K. A. Browning, C. J. Morcrette, A. M. Blyth, R. M. Forbes, B. Brooks, and F. Perry, 2014: The evolution of an MCS over southern England. Part 1: Observations. *Quart. J. Roy. Meteor. Soc.,* **140,** 439–457, doi:10.1002/qj.2138.

Coleman, T. A., and K. R. Knupp, 2009: Factors affecting surface wind speeds in gravity waves and wake lows. *Wea. Forecasting,* **24,** 1664–1679, doi:10.1175/2009WAF2222248.1.

——, and ——, 2010: A nonlinear impedance relation for the surface winds in pressure disturbances. *J. Atmos. Sci.,* **67,** 3409–3422, doi:10.1175/2010JAS3457.1.

Crook, N. A., 1988: Trapping of low-level internal gravity waves. *J. Atmos. Sci.,* **45,** 1533–1541, doi:10.1175/1520-0469(1988)045<1533:TOLLIG>2.0.CO;2.

Dai, A., and J. Wang, 1999: Diurnal and semidiurnal tides in global surface pressure fields. *J. Atmos. Sci.,* **56,** 3874–3891, doi:10.1175/1520-0469(1999)056<3874:DASTIG>2.0.CO;2.

de Groot-Hedlin, C. D., M. A. Hedlin, and K. T. Walker, 2014: Detection of gravity waves across the USArray: A case study. *Earth Planet. Sci. Lett.,* **402,** 346–352, doi:10.1016/j.epsl.2013.06.042.

de Pondeca, M., and Coauthors, 2011: The real-time mesoscale analysis at NOAA's National Centers for Environmental

Prediction: Current status and development. *Wea. Forecasting,* **26,** 593–612, doi:10.1175/WAF-D-10-05037.1.

Dirren, S., R. D. Torn, and G. J. Hakim, 2007: A data assimilation case study using a limited-area ensemble Kalman filter. *Mon. Wea. Rev.,* **135,** 1455–1473, doi:10.1175/MWR3358.1.

Einaudi, F., A. J. Bedard, and J. J. Finnigan, 1989: A climatology of gravity waves and other coherent disturbances at the Boulder Atmospheric Observatory during March–April 1984. *J. Atmos. Sci.,* **46,** 303–329, doi:10.1175/1520-0469(1989)046<0303:ACOGWA>2.0.CO;2.

Engerer, N. A., D. J. Stensrud, and M. C. Coniglio, 2008: Surface characteristics of observed cold pools. *Mon. Wea. Rev.,* **136,** 4839–4849, doi:10.1175/2008MWR2528.1.

Fujita, T. T., and H. A. Brown, 1958: A study of mesosystems and their radar echoes. *Bull. Amer. Meteor. Soc.,* **39,** 538–554.

Gaberšek, S., and D. R. Durran, 2006: Gap flows through idealized topography. Part II: Effects of rotation and surface friction. *J. Atmos. Sci.,* **63,** 2720–2739, doi:10.1175/JAS3786.1.

Geerts, B., Q. Miao, and J. C. Demko, 2008: Pressure perturbations and upslope flow over a heated, isolated mountain. *Mon. Wea. Rev.,* **136,** 4272–4288, doi:10.1175/2008MWR2546.1.

Grivet-Talocia, S., and F. Einaudi, 1998: Wavelet analysis of a microbarograph network. *IEEE Trans. Geosci. Remote Sens.,* **36,** 418–433, doi:10.1109/36.662727.

——, ——, W. L. Clark, R. D. Dennett, G. D. Nastrom, and T. E. VanZandt, 1999: A 4-yr climatology of pressure disturbances using a barometer network in central Illinois. *Mon. Wea. Rev.,* **127,** 1613–1629, doi:10.1175/1520-0493(1999)127<1613:AYCOPD>2.0.CO;2.

Horel, J., and Coauthors, 2002: Mesowest: Cooperative mesonets in the western United States. *Bull. Amer. Meteor. Soc.,* **83,** 211–225, doi:10.1175/1520-0477(2002)083<0211:MCMITW>2.3.CO;2.

Jewett, B. F., M. K. Ramamurthy, and R. M. Rauber, 2003: Origin, evolution, and finescale structure of the St. Valentine's Day mesoscale gravity wave observed during STORM-FEST. Part III: Gravity wave genesis and the role of evaporation. *Mon. Wea. Rev.,* **131,** 617–633, doi:10.1175/1520-0493(2003)131<0617:OEAFSO>2.0.CO;2.

Johns, R. H., and W. D. Hirt, 1987: Derechos: Widespread convectively induced windstorms. *Wea. Forecasting,* **2,** 32–49, doi:10.1175/1520-0434(1987)002<0032:DWCIW>2.0.CO;2.

Johnson, R. H., 2001: Surface mesohighs and mesolows. *Bull. Amer. Meteor. Soc.,* **82,** 13–31, doi:10.1175/1520-0477(2001)082<0013:SMAM>2.3.CO;2.

Jones, P. D., T. J. Osborn, and K. R. Briffa, 2003: Pressure-based measures of the North Atlantic Oscillation (NAO): A comparison and an assessment of changes in the strength of the NAO and in its influence on surface climate parameters. *The North Atlantic Oscillation: Climatic Significance and Environmental Impact,* J. W. Hurrell et al., Eds., Amer. Geophys. Union, 173–192.

Koch, S. E., and C. O'Handley, 1997: Operational forecasting and detection of mesoscale gravity waves. *Wea. Forecasting,* **12,** 253–281, doi:10.1175/1520-0434(1997)012<0253:OFADOM>2.0.CO;2.

——, and L. M. Siedlarz, 1999: Mesoscale gravity waves and their environment in the central United States during STORM-FEST. *Mon. Wea. Rev.,* **127,** 2854–2879, doi:10.1175/1520-0493(1999)127<2854:MGWATE>2.0.CO;2.

——, and S. Saleeby, 2001: An automated system for the analysis of gravity waves and other mesoscale phenomena. *Wea. Forecasting,* **16,** 661–679, doi:10.1175/1520-0434(2001)016<0661:AASFTA>2.0.CO;2.

Koppel, L. L., L. F. Bosart, and D. Keyser, 2000: A 25-yr climatology of large-amplitude hourly surface pressure changes over the conterminous United States. *Mon. Wea. Rev.,* **128,** 51–68, doi:10.1175/1520-0493(2000)128<0051:AYCOLA>2.0.CO;2.

Krueger, O., and H. von Storch, 2012: The informational value of pressure-based single-station proxies for storm activity. *J. Atmos. Oceanic Technol.,* **29,** 569–580, doi:10.1175/JTECH-D-11-00163.1.

Lee, X., and A. G. Barr, 1998: Climatology of gravity waves in a forest. *Quart. J. Roy. Meteor. Soc.,* **124,** 1403–1419, doi:10.1002/qj.49712454904.

Li, Y., and R. B. Smith, 2010: The detection and significance of diurnal pressure and potential vorticity anomalies east of the Rockies. *J. Atmos. Sci.,* **67,** 2734–2751, doi:10.1175/2010JAS3423.1.

Madaus, L. E., G. J. Hakim, and C. F. Mass, 2014: Utility of dense pressure observations for improving mesoscale analyses and forecasts. *Mon. Wea. Rev.,* **142,** 2398–2413, doi:10.1175/MWR-D-13-00269.1.

Markowski, P., and Y. Richardson, 2010: *Mesoscale Meteorology in Midlatitudes.* John Wiley & Sons, Ltd., 399 pp.

Mass, C. F., and L. E. Madaus, 2014: Surface pressure observations from smartphones: A potential revolution for high-resolution weather prediction? *Bull. Amer. Meteor. Soc.,* **95,** 1343–1349, doi:10.1175/BAMS-D-13-00188.1.

——, W. J. Steenburgh, and D. M. Schultz, 1991: Diurnal surface-pressure variations over the continental United States and the influence of sea level reduction. *Mon. Wea. Rev.,* **119,** 2814–2830, doi:10.1175/1520-0493(1991)119<2814:DSPVOT>2.0.CO;2.

Metz, N. D., and L. F. Bosart, 2010: Derecho and MCS development, evolution, and multiscale interactions during 3–5 July 2003. *Mon. Wea. Rev.,* **138,** 3048–3070, doi:10.1175/2010MWR3218.1.

Nappo, C., 2002: *An Introduction to Atmospheric Gravity Waves.* International Geophysics Series, Vol. 85, Academic Press, 276 pp.

National Weather Service Weather Forecast Office cited, 2014: Squall line produces wind damage and large hail June 13th, 2013. Blacksburg, VA. [Available online at http://www.erh.noaa.gov/rnk/events/2013/June13th_SquallLine/summary.php.]

Nieto Ferreira, R., L. Hall, and T. M. Rickenbach, 2013: A climatology of the structure, evolution, and propagation of midlatitude cyclones in the southeast United States. *J. Climate,* **26,** 8406–8421, doi:10.1175/JCLI-D-12-00657.1.

Novak, D. R., and B. A. Colle, 2006: Observations of multiple sea breeze boundaries during an unseasonably warm day in metropolitan New York City. *Bull. Amer. Meteor. Soc.,* **87,** 169–174, doi:10.1175/BAMS-87-2-169.

Orlanski, I., 1975: A rational subdivision of scales for atmospheric processes. *Bull. Amer. Meteor. Soc.,* **56,** 527–530.

Pavlis, G. L., K. Sigloch, S. Burdick, M. J. Fouch, and F. Vernon, 2012: Unraveling the geometry of the Farallon Plate: Synthesis of three-dimensional imaging results from the USArray. *Tectonophysics,* **532–535,** 82–102, doi:10.1016/j.tecto.2012.02.008.

Ramamurthy, M. K., R. M. Rauber, B. P. Collins, and N. K. Malhotra, 1993: A comparative study of large-amplitude gravity-wave events. *Mon. Wea. Rev.,* **121,** 2951–2974, doi:10.1175/1520-0493(1993)121<2951:ACSOLA>2.0.CO;2.

Ray, R. D., and S. Poulose, 2005: Terdiurnal surface-pressure oscillations over the continental United States. *Mon. Wea. Rev.,* **133,** 2526–2534, doi:10.1175/MWR2988.1.

Reitan, C. H., 1974: Frequencies of cyclones and cyclogenesis for North America, 1951–1970. *Mon. Wea. Rev.,* **102,** 861–868, doi:10.1175/1520-0493(1974)102<0861:FOCACF>2.0.CO;2.

Ruppert, J. H., and L. F. Bosart, 2014: A case study of the interaction of a mesoscale gravity wave with a mesoscale convective system. *Mon. Wea. Rev.,* **142,** 1403–1429, doi:10.1175/MWR-D-13-00274.1.

Sanders, F., and J. R. Gyakum, 1980: Synoptic-dynamic climatology of the ''bomb.'' *Mon. Wea. Rev.,* **108,** 1589–1606, doi:10.1175/1520-0493(1980)108<1589:SDCOT>2.0.CO;2.

Sutherland, B., 2010: *Internal Gravity Waves.* Cambridge University Press, 377 pp.

Thomas, B. C., and J. E. Martin, 2007: A synoptic climatology and composite analysis of the Alberta clipper. *Wea. Forecasting,* **22,** 315–333, doi:10.1175/WAF982.1.

Tian, W., D. J. Parker, S. Mobbs, M. Hill, C. A. D. Kilburn, and D. Ladd, 2004: Observing coherent boundary layer motions using remote sensing and surface pressure measurement. *J. Atmos. Oceanic Technol.,* **21,** 1481–1490, doi:10.1175/1520-0426(2004)021<1481:OCBLMU>2.0.CO;2.

Torrence, C., and G. P. Compo, 1998: A practical guide to wavelet analysis. *Bull. Amer. Meteor. Soc.,* **79,** 61–78, doi:10.1175/1520-0477(1998)079<0061:APGTWA>2.0.CO;2.

Tyndall, D., and J. Horel, 2013: Impacts of mesonet observations on meteorological surface analyses. *Wea. Forecasting,* **28,** 254–269, doi:10.1175/WAF-D-12-00027.1.

Tytell, J. E., J. Eakins, and F. Vernon, 2011: Tracking outflows from severe thunderstorms using NSF EarthScope USArray pressure sensors. *24th Conf. on Weather and Forecasting/20th Conf. on Numerical Weather Prediction,* Seattle, WA, Amer. Meteor. Soc., 2A.3. [Available online at https://ams.confex.com/ams/91Annual/webprogram/Manuscript/Paper180739/AMS_2011_JonTytell_Extended_abstract.pdf.]

Vernon, F. L., J. Eakins, J. Tytell, M. Hedlin, B. Busby, and B. Woodward, 2011: Observations of weather phenomena by NSF EarthScope USArray seismic and pressure sensors. *24th Conf. on Weather and Forecasting/20th Conf. on Numerical Weather Prediction,* Seattle, WA, Amer. Meteor. Soc., P110. [Available online at https://ams.confex.com/ams/91Annual/webprogram/Manuscript/Paper180671/AMS_2011_FrankVernon_Extended_abstract.pdf.]

——, J. E. Tytell, B. Busby, J. Eakins, M. Hedlin, A. Muschinski, K. Walker, and B. Woodward, 2012: Scientific viability of the USArray Transportable Array network as a real-time weather monitoring platform. *16th Symp. on Meteorological Observation and Instrumentation,* New Orleans, LA, Amer. Meteor. Soc., 5.3. [Available online at https://ams.confex.com/ams/92Annual/webprogram/Manuscript/Paper200044/AMS_2012_FrankV_Extended_abstract.pdf.]

Viana, S., E. Terradellas, and C. Yagüe, 2010: Analysis of gravity waves generated at the top of a drainage flow. *J. Atmos. Sci.,* **67,** 3949–3966, doi:10.1175/2010JAS3508.1.

Wei, J., and F. Zhang, 2014: Mesoscale gravity waves in moist baroclinic jet–front systems. *J. Atmos. Sci.,* **71,** 929–952, doi:10.1175/JAS-D-13-0171.1.

Wheatley, D. M., and D. J. Stensrud, 2010: The impact of assimilating surface pressure observations on severe weather events in a WRF mesoscale ensemble system. *Mon. Wea. Rev.,* **138,** 1673–1694, doi:10.1175/2009MWR3042.1.

Whitaker, J. S., G. P. Compo, X. Wei, and T. M. Hamill, 2004: Reanalysis without radiosondes using ensemble data assimilation. *Mon. Wea. Rev.,* **132,** 1190–1200, doi:10.1175/1520-0493(2004)132<1190:RWRUED>2.0.CO;2.

Yang, Y., and M. H. Ritzwoller, 2008: Teleseismic surface wave tomography in the western U.S. using the transportable array component of USArray. *Geophys. Res. Lett.,* **35,** L04308, doi:10.1029/2007GL032278.

Zishka, K. M., and P. J. Smith, 1980: The climatology of cyclones and anticyclones over North America and surrounding ocean environs for January and July, 1950–77. *Mon. Wea. Rev.,* **108,** 387–401, doi:10.1175/1520-0493(1980)108<0387:TCOCAA>2.0.CO;2.